



HAL
open science

Elastic bound state in the continuum with perfect mode conversion

Liyun Cao, Yifan Zhu, Yanlong Xu, Shi-Wang Fan, Zhichun Yang, B. Assouar

► To cite this version:

Liyun Cao, Yifan Zhu, Yanlong Xu, Shi-Wang Fan, Zhichun Yang, et al.. Elastic bound state in the continuum with perfect mode conversion. *Journal of the Mechanics and Physics of Solids*, 2021, 154, pp.104502. 10.1016/j.jmps.2021.104502 . hal-03412431

HAL Id: hal-03412431

<https://hal.science/hal-03412431>

Submitted on 15 Nov 2021

HAL is a multi-disciplinary open access archive for the deposit and dissemination of scientific research documents, whether they are published or not. The documents may come from teaching and research institutions in France or abroad, or from public or private research centers.

L'archive ouverte pluridisciplinaire **HAL**, est destinée au dépôt et à la diffusion de documents scientifiques de niveau recherche, publiés ou non, émanant des établissements d'enseignement et de recherche français ou étrangers, des laboratoires publics ou privés.



Distributed under a Creative Commons Attribution - NonCommercial - NoDerivatives 4.0 International License

Elastic Bound State in the Continuum with Perfect Mode Conversion

Liyun Cao^{1,2}, Yifan Zhu², Yanlong Xu¹, Shi-Wang Fan², Zhichun Yang^{1,*}, and Badreddine Assouar^{2,*}

¹*School of Aeronautics, Northwestern Polytechnical University, Xi'an, 710072, China*

²*Institut Jean Lamour, CNRS, Université de Lorraine, Nancy, 54506, France*

*Corresponding author e-mails: yangzc@nwpu.edu.cn & badreddine.assouar@univ-lorraine.fr

Abstract

The partial or complete confinement of waves in an open system is omnipresent in nature and in wave-based materials and technology. Here, we theoretically analyze and experimentally observe the formation of a trapped mode with perfect mode conversion (TMPC) between flexural waves and longitudinal waves, by achieving a quasi-bound state in the continuum (BIC) in an open elastic wave system. The latter allows a quasi-BIC in a semi-infinite background plate when Fano resonance hybridizes flexural and longitudinal waves and balances their radiative decay rates. We demonstrate that when the Fabry-Pérot resonance of the longitudinal wave is realized simultaneously, the TMPC formed by the elastic BIC approaches infinite quality factor. Furthermore, we show that quasi-BIC can be tuned continuously to BIC through the critical frequency of mode conversion, which offers the possibility of TMPC with an arbitrarily high quality factor. Our reported concept and physical mechanism open new routes to achieve perfect mode conversion with tunable high quality factor in elastic systems.

Introduction

Bound states in the continuum (BICs), defying the conventional bound states located outside the continuum, are non-decaying localized states embedded within the continuous spectrum of radiating waves (Hsu et al., 2016; Kodigala et al., 2017). The states can sometimes be regarded as embedded eigenvalues (Hsu et al., 2016) or embedded trapped modes (Hsu et al., 2013b) with infinite quality factors. The BIC concept was first proposed in quantum mechanics (von Neumann and Wigner, 1993) by mathematically constructing a 3D potential extending to infinity. Since this initial proposal, the wave phenomenon of BICs has been identified in different material and wave systems (Hsu et al., 2016), such as electromagnetic waves (Hsu et al., 2013b; Kodigala et al., 2017; Koshelev et al., 2019; Marinica et al., 2008; Minkov et al., 2018; Plotnik et al., 2011; Zhen et al., 2014), acoustic waves in the air (Cumpsty and Whitehead, 1971; Huang et al., 2020; Lyapina et al., 2018; Parker and Griffiths, 1968), water waves (Callan et al., 1991; Cobelli et al., 2011) and surface acoustic waves (Kawachi et al., 2001; Lim and Farnell, 1969; Trzupek and Zieliński, 2009) in semi-infinite media. Structures supporting BICs or quasi-BICs with high quality factor (high-Q) have been widely studied and opened the route to numerous applications in different fields, especially in optics and photonics, such as lasers (Hirose et al., 2014; Imada et al., 1999; Lin et al., 2020; Matsubara et al., 2008; Noda et al., 2001), sensors (Romano et al., 2019; Yanik et al., 2011; Zhen et al., 2013), and filters (Doskolovich et al., 2019; Foley et al., 2014; Ju et al., 2020).

Compared to the optical and acoustic BICs, the elastic counterpart is rarely

concerned due to its more sophisticated polarization states (Graff, 1975; Rose, 1999). Recently some works have investigated elastic BICs in elastodynamics. Elastic BIC of bulk waves (Haq and Shabanov, 2021) was studied using the Fabry-Perot mirroring mechanism in an infinite solid with mixed in-plane polarizations. Non-symmetry-protected BICs of surface acoustic waves (Maznev and Every, 2018) and symmetry-protected ones (Lim and Farnell, 1969; Trzupiek and Zieliński, 2009) have also been investigated in semi-infinite solids with surface polarization. However, most of those BIC-supporting models have never been experimentally witnessed. So far, in structural dynamics, especially for flexural and longitudinal waves (Graff, 1975; Rose, 1999) in common plate-like structures, the researches on elastic BICs have still not been reported.

On the other hand, perfect mode conversion (Giurgiutiu, 2007; Graff, 1975; Rose, 1999) between different polarization modes has grown into a burgeoning research area in the elastic wave system, due to its potential wide applications in nondestructive testing, medical ultrasonography, and earthquake resistance in civil engineering. For example, a mode-coupled layer with the balanced mode excitations and diagonal polarizations (Kweun et al., 2017) can achieve maximum mode conversion between longitudinal and shear modes, promoting the development of sensors in industrial and biomedical testing (Yang and Kim, 2018; Yang et al., 2019; Zheng et al., 2020). Pillared seismic metamaterials (Colombi et al., 2016a; Colombi et al., 2016b; Colquitt et al., 2017) can create effective bandgaps to achieve mode conversion from surface waves to bulk waves, promoting civil structures against seismic risk. Here, we propose a theoretical method to achieve perfect mode conversion between flexural waves (out-

plane vibration) and longitudinal waves (in-plane vibration) (Graff, 1975; Rose, 1999) in two perpendicular polarization planes, which has never been reported. The new elastic-wave mode conversion mechanism enriches the form of elastic wave energy flow, which can perfectly convert an in-plane test signal or in-plane vibration energy into an out-plane one for the simplifications of nondestructive testing or energy harvesting, perfectly convert an out of plane vibration into in-plane one for reducing vibration.

In this research, we present theoretical analysis and experimental evidence of achieving a trapped mode with perfect mode conversion (TMPC) in a quasi-BIC-supporting elastic wave system. In the proposed scheme, Fano resonance hybridizes flexural and longitudinal waves in two perpendicular polarization planes and converts one mode into another. When the radiative decay rate of the converted mode balances that of the directly reflected wave from the incident wave entering the system, the incident wave will be completely trapped by the hybrid Fano resonance, i.e., quasi-BIC. The resonant system only allows the converted mode to leak, leading to perfect mode conversion. Furthermore, we prove that TMPC can support infinite-Q BIC by simultaneously achieving the hybrid Fano and Fabry-Pérot resonances. We demonstrate that all quasi-BICs can be continuously tuned to BICs when the critical frequency of the mode conversion, depending on the incident angle, approaches the Fano resonance one.

2. Theory and results

To clearly show the unique TMPC in the quasi-BIC-supporting and BIC-

supporting elastic wave systems, we investigate a simple structure with typical resonance characteristics. The structure is composed of a periodic waveguide resonator with the length s on the edge of a background plate with infinite left boundary, as shown in Fig. 1(a). These waveguide resonators are connected to side-coupled pillared resonators with the height h . The thicknesses d of the waveguide resonator and pillared resonator are in deep subwavelength scale relative to the wavelength in the whole considered frequency range. Only the fundamental modes of flexural waves and longitudinal waves are involved.

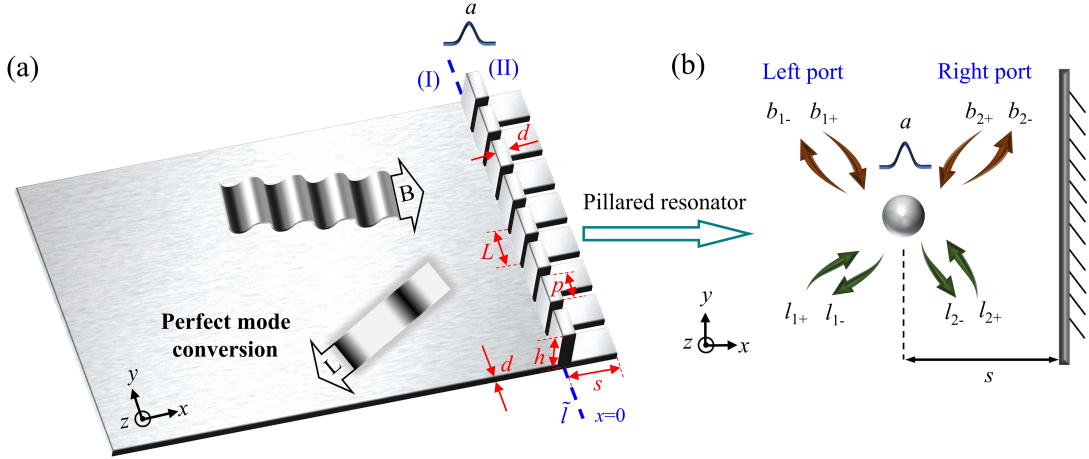


Fig. 1. (a) A Fano-resonance-supporting elastic wave model: periodic waveguide with the length s connected to a side-coupled pillared resonator with the height h , on the edge of a semi-infinite background plate with the thickness d . The Fano resonance hybridizes flexural wave (bending wave) “B” and longitudinal wave “L” with polarizations in the x - z plane and x - y plane (perpendicular one), respectively. The resonance system perfectly converts one mode into another. (b) Schematic illustrations for the set-up of temporal coupled-mode theory in a subunit. The localized mode has amplitude a , which hybridizes the incoming flexural waves with amplitudes b_{1+} , b_{2+} , incoming longitudinal waves with amplitudes l_{1+} , l_{2+} , outgoing flexural waves with amplitudes b_{1-} , b_{2-} ,

and outgoing longitudinal waves with amplitudes l_{1-} , l_{2-} , respectively.

2.1. Analytical model of side-coupled pillared resonators with the Fano resonance and the hybridization coupling

As illustrated in the schematic of Fig. 1(b), the pillared resonator can hybridize the flexural and longitudinal waves in the background plate. First, without considering the right boundary, we get the scattering equation of the pillared resonator in the far-field as

$$\mathbf{S}^- = \begin{bmatrix} t_b & r_b & t_{lb} & -r_{lb} \\ r_b & t_b & r_{lb} & -t_{lb} \\ t_{bl} & -r_{bl} & t_l & r_l \\ r_{bl} & -t_{bl} & r_l & t_l \end{bmatrix} \mathbf{S}^+ = \mathbf{M}_p \cdot \mathbf{S}^+, \quad (1)$$

where $\mathbf{S}^- = [b_{2-}, b_{1-}, l_{2-}, l_{1-}]^T$ and $\mathbf{S}^+ = [b_{1+}, b_{2+}, l_{1+}, l_{2+}]^T$ are scattering vectors. \mathbf{M}_p is the scattering matrix. The symbols t and r denote the transmission and reflection coefficients, respectively. The subscripts b and l represent the flexural wave (or bending wave) and longitudinal wave. The subscripts bl and lb represent the conversion from flexural wave to longitudinal wave and the reverse process, respectively. Analytical expressions of all scattering coefficients in the scattering matrix \mathbf{M}_p are obtained by the transfer matrix method (see detailed derivation in Appendix A).

In the following, we study the case that the pillared resonator and the waveguide resonator have the same flexural rigidity, i.e., the same thickness, providing a strong hybridization coupling (Colquitt et al., 2017). The material parameters of the model are obtained based on the experimental measurement of 3D printing material PLA (see Appendix F). Figs. 2(a) and 2(b) display the dimensionless scattering energy curves for

the incident flexural wave, based on the scattering coefficients in Eq. (1) (see details in Appendix A) and the full wavefield simulations (see details in Appendix H), respectively. This consistency between Figs. 2(a) and 2(b) verifies the correctness of the analytical model. Another important verification is the power flow balance, i.e., the total energy of all scattering modes e_i is unit (grey dot line). We note that the reflection energy curve e_{r_b} has a clear Fano profile. The Fano profile is a typical feature of the Fano resonance (Fano, 1961; Rupin et al., 2014), which is the result of the interference between the flexural resonances of the pillared resonator and the incident flexural waves. The Fano resonance frequency ω_0 [marked by yellow dashed lines in Fig. 2(a)], dominated by the flexural resonance, approximately satisfies the transcendental equation (Colquitt et al., 2017; Graff, 1975)

$$\cos(h\beta\sqrt{\omega_0}) \cdot \cosh(h\beta\sqrt{\omega_0}) = -1, \quad (2)$$

where β is the propagation constant, $\beta^4 = \rho d/D$, and D is the bending rigidity.

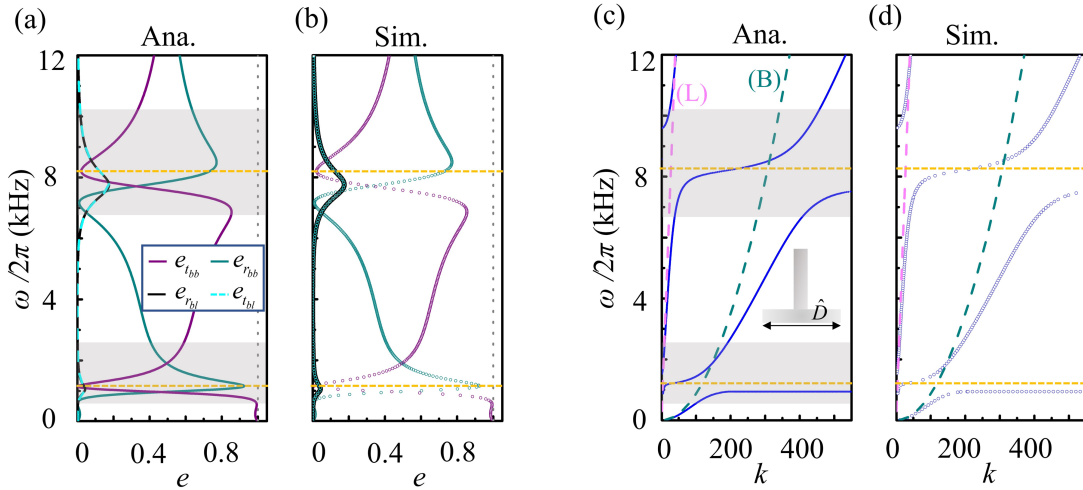


Fig. 2. (a) and (b) The dimensionless scattering energy curves for the incident flexural wave in the background plate without the boundary, based on the analytical and simulated methods, respectively.

The grey dot line represents the total energy of all scattering modes. The yellow dashed lines indicate

Fano resonance frequency. (c) and (d) Frequency–wavenumber representations correspond to the band structures for the pillared resonator, based on the analytical and simulated methods, respectively. The dispersion curves of the flexural wave (green dashed line) and longitudinal one (pink dashed line) in the background plate are superimposed.

Based on the analytical model, we analyze its band structure to intuitively show the hybridization coupling between flexural waves and longitudinal waves from the Fano resonance. Bloch boundary condition can be expressed as

$$T_R = e^{ik\hat{D}} I \cdot T_L, \quad (3)$$

where I is the identity matrix and \hat{D} is a typical period with a quarter wavelength in the second Fano resonance frequency. $T_L = [b_{1+}, b_{1-}, b_{1+}^*, b_{1-}^*, l_{1+}, l_{1-}]$ and $T_R = [b_{2-}, b_{2+}, b_{2-}^*, b_{2+}^*, l_{2-}, l_{2+}]$ are the transmission vectors in the left and right of the pillared resonator, respectively, where the subscript $*$ represents the evanescent flexural wave in the near field. According to Eqs. (1) and (3), the band structure can be calculated by

$$\left| \mathbf{M}_p^* - \begin{pmatrix} e^{ik_b\hat{D}} & & & & & \\ & e^{-ik_b\hat{D}} & & & & \\ & & e^{k_b\hat{D}} & & & \\ & & & e^{-k_b\hat{D}} & & \\ & & & & e^{-ik_l\hat{D}} & \\ & & & & & e^{-ik_l\hat{D}} \end{pmatrix} \right| = 0, \quad (4)$$

where \mathbf{M}_p^* is the scattering matrix, including the phase origins and evanescent flexural modes (see Appendix A). Based on Eq. (4), Fig. 2(c) displays the band structure (blue lines), which is very consistent with the simulated one in Fig. 2(d). The

dispersion curves of the flexural wave (green dashed line) and longitudinal wave (pink dashed line) in the background plate are superimposed. Around marked first and second Fano resonances [gray areas in Fig. 2(b)], the band structures have typical three hybridized branches (blue lines): the right lower and left upper ones corresponding to the hybridized flexural and longitudinal modes, respectively; and the one in-between corresponding to the third mode of mixed symmetry (Rupin et al., 2014; Rupin and Roux, 2017). The three hybridized branches show strong mode coupling between flexural waves and longitudinal waves around Fano resonances.

2.2. The destructive interference relation based on the waveguide resonator

The introduction of the right waveguide resonator with the length s , as shown in Fig. 1, reshapes the interference of the incident flexural waves. The length s is greater than half of the wavelength in the resonance frequency, eliminating the influence of evanescent flexural waves from the near field. The Fano resonance leaks the left scattering flexural waves into the background plate (channel one), and the right scattering flexural waves into the waveguide resonator. The right boundary of the waveguide resonator reflects all the right-going flexural waves, and part of that is transmitted through the pillared resonator into the background plate (channel two), interfering with channel one. Destructive interference can eliminate the radiation of flexural waves in these two channels to emerge a local state.

In the above intuitive understanding of the physical origin of the destructive interference, the coupling between the scattering modes of the resonance is an essential

element. To theoretically explore the destructive interference in the elastic wave system, we expand the temporal coupled-mode theory (Fan et al., 2003; Hsu et al., 2013a; Hsu et al., 2013b) in optics, which provides a simple analytical description for resonant objects weakly coupled to incoming and outgoing propagation modes. As shown in Fig. 1(b), the amplitude a of the localized mode evolves as $da/dt = (-i\omega_0 - \gamma_0)a$ in the absence of input powers. γ_0 is the radiative decay rate of the localized mode. The temporal coupled-mode theory for coupling between the resonance and incoming and outgoing propagation modes can be described (Fan et al., 2003) as

$$\mathbf{s}_- = C \cdot \mathbf{s}_+ + a \cdot \mathbf{d} \quad (5)$$

where $\mathbf{s}_+ = [b_{1+} \ b_{2+} \ l_{1+} \ l_{2+}]^T$ and $\mathbf{s}_- = [b_{1-} \ b_{2-} \ l_{1-} \ l_{2-}]^T$ are the incoming and outgoing propagation vectors, as shown in Fig. 1(b). $\mathbf{d} = [\bar{d}_1 \ \bar{d}_2 \ \bar{d}_3 \ \bar{d}_4]^T$ is the coupling vector at the ports, where \bar{d}_1 and \bar{d}_2 represent coupling coefficients between the localized mode and the incoming propagation flexural wave at the right and left ports, respectively. \bar{d}_3 and \bar{d}_4 represent coupling coefficients between the localized mode and the incoming longitudinal wave at the right and left ports,

respectively. The scattering matrix $C = \begin{pmatrix} 0 & 1 & 0 & 0 \\ 1 & 0 & 0 & 0 \\ 0 & 0 & 0 & 1 \\ 0 & 0 & 1 & 0 \end{pmatrix}$ describes the incoming and

outgoing waves in the ports couple through a direct pathway, i.e., ignoring the resonance-assisted coupling.

As shown in Fig. 1(b), according to Eq. (5), we can understand that the radiation of $\bar{d}_1 \cdot a$ is from the coupling between the localized mode and the incoming propagation flexural modes at the right port. The radiation will leak into the left port

and includes the leakages of the flexural wave and the longitudinal one from mode conversion. Based on the scattering coefficient in Eq. (1), the leakages of the flexural wave and the converted longitudinal one in the left port can be expressed as $t_b b_{2+} - b_{2+}$ and $t_{lb} l_{2+}$, respectively. Therefore, we can get the relationship between the localized mode and the leakages in the left port:

$$\bar{d}_1 \cdot a = t_b b_{2+} - b_{2+} + t_{lb} l_{2+}. \quad (6)$$

Similarly, we can get the relationship in the right port:

$$\bar{d}_2 a = r_b b_{2+} + r_{lb} l_{2+}. \quad (7)$$

The incident propagating modes b_{1+} are not taken into account (Hsu et al., 2016). With the propagation relation of $b_{2-} = e^{-i\phi} \cdot b_{2+}$, according to Eqs. (5)-(7) and (A17), we can get the analytical expression of the destructive interference relation as

$$e^{-i\phi} = t_b + r_b, \quad (8)$$

where $\phi = 2k_b s - 3\pi/2$ is a phase shift of one round-trip of flexural waves in the waveguide, and k_b is the wavenumber of the flexural wave. On the other hand, considering an incident positive-going flexural wave of $1 \cdot e^{i\omega t}$, the transmitted and reflected longitudinal waves from the mode conversion have a reverse polarization direction. These longitudinal waves will interfere and cancel at the scattering source (the resonator), based on Eq. (A10). Therefore, at the scattering source, the total scattering field is the superposition of the transmitted and reflected flexural waves with the same polarization direction, i.e., $r_b + t_b$. According to the energy conservation, the energy of the total scattering field equal to that of the incident wave field. We can obtain the amplitude relationship of the total scattering field $r_b + t_b$ as

$$|r_b + t_b|^2 = 1. \quad (9)$$

In such case, the magnitude condition of Eq. (8) is always satisfied, and Eq. (8) can be reduced as its phase relation:

$$2\beta\sqrt{\omega s} - \frac{3\pi}{2} = \arg(r_b + t_b) + 2n\pi, \quad (10)$$

where n is a positive integer.

We should point out that hybridization coupling is an essential component of these unique local states from destructive interference. The reason is that the wave fields in the system only have one mode without mode hybridization, then any state must be leaky. The radiative energy from mode conversion in our system is similar to dissipative loss in the optical resonance system (Hsu et al., 2016). But the “dissipative loss” in our study can be adjusted by the waveguide resonator, which will be discussed in detail later.

2.3. Analytical model of the whole resonator system

To evaluate all possible localized states in the parameter space, we establish the analytical model of the whole resonator system. As shown in Fig. 1(a), the background plate, the pillared resonator, and the waveguide resonator are divided into region (I) and region (II) by the dividing line \tilde{l} . For the sake of universality to study the vertically and obliquely incident waves in the background plate, the governing equations for the flexural and longitudinal waves in the region (I) should be written in the two-dimension form:

$$w^{(I)}(x, y) = A_0 e^{-ik_b^y \cdot y} e^{-ik_b^x \cdot x} + R_b e^{-ik_b^y \cdot y} e^{ik_b^x \cdot x} + R_b^* e^{-ik_b^y \cdot y} e^{\hat{k}_b^x \cdot x}, \quad (11)$$

$$u^{(I)}(x, y) = R_{bl} e^{-ik_l^y \cdot y} e^{ik_l^x \cdot x}, \quad (12)$$

, respectively, where A_0 is the amplitude of the incident flexural wave, R_b , R_b^* , and R_{bl} are the complex coefficients of the reflected propagating flexural wave, reflected evanescent flexural wave, and reflected longitudinal wave, respectively. k_b^y and k_l^y are y -component wave vectors of propagating flexural waves and longitudinal waves, respectively. According to the conservation of parallel wave vectors, we can get $k_b^y = k_l^y = \sin\theta_i \cdot k_b$, where θ_i is the incident angle. $k_b^x = \sqrt{(k_b)^2 - (k_b^y)^2}$ and $\hat{k}_b^x = -i\sqrt{-(k_b)^2 - (k_b^y)^2}$ are x -component wave vectors of propagating and evanescent flexural waves, respectively. $k_l^x = \sqrt{(k_l)^2 - (k_l^y)^2}$ is x -component wave vector of longitudinal waves. The coefficient vector of the reflected scattering field in the region (I) can be defined as $\mathbf{T}_r^{(I)} = [R_b \quad R_b^* \quad R_{bl}]^T$.

The hybrid resonant system consists of the pillared and waveguide resonators. Only the fundamental mode needs to be taken into account since the widths p and thicknesses d of the waveguide and pillar are in deep subwavelength scale. The coefficient vector of the wavefield at the left interface of the waveguide resonator (the right of the dividing line \tilde{l}) can be defined as $\mathbf{T}^{(II)} = [a_2 \quad b_2 \quad c_2 \quad d_2 \quad e_2 \quad f_2]^T$, where a_2 and b_2 correspond to the complex coefficients of the positive-going propagating and evanescent flexural waves in the waveguide resonator. c_2 and d_2 correspond to the complex coefficients of the negative-going propagating and evanescent flexural waves. e_2 and f_2 correspond to the complex coefficients of the positive-going and negative-going propagating longitudinal waves.

In the x -direction of Fig. 1(a), the slope φ , bending moment M , shear force V , and axial force F in the two-dimension plate model of the region (I) are expressed as

$$\varphi_x^{(i)} = \frac{\partial w^{(i)}}{\partial x}, \quad (13)$$

$$M_x^{(i)} = \begin{cases} D\left(\frac{\partial^2 w^{(i)}}{\partial x^2} + \nu \frac{\partial^2 w^{(i)}}{\partial y^2}\right) & y - y_j \leq |p/2|, \\ 0 & y - y_j + L/2 \leq |(L-p)/2| \end{cases}, \quad (14)$$

$$V_x^{(i)} = \begin{cases} -D\left(\frac{\partial^3 w^{(i)}}{\partial x^3} + \frac{\partial^3 w^{(i)}}{\partial x \partial y^2}\right) & y - y_j \leq |p/2|, \\ 0 & y - y_j + L/2 \leq |(L-p)/2| \end{cases}, \quad (15)$$

$$F_x^{(i)} = \begin{cases} \frac{Ed}{1-\nu^2} \cdot \frac{\partial u^{(i)}}{\partial x} & y - y_j \leq |p/2|, \\ 0 & y - y_j + L/2 \leq |(L-p)/2| \end{cases}, \quad (16)$$

where $y_j = (j-1)L$, and j denotes the j^{th} subunit.

By applying the continuous boundary condition of x -components of the flexural wave displacement at the left interface of waveguide $x=0$ and integrating along y -direction in the region $y - y_j \leq |p/2|$, we can get

$$\mu g \cdot A_0 + [\mu g \quad \mu g \quad 0] \mathbf{T}_r^{(i)} = [1 \quad 1 \quad 1 \quad 1 \quad 0 \quad 0] \mathbf{T}^{(ii)}, \quad (17)$$

where $g = \text{sinc}(k_b^y \cdot p/2)$ and $\mu = e^{-ik_b^y \cdot y_j}$. In the same way, applying the continuous boundary condition of the slop at the interface of $x=0$, we can get

$$-ik_b^x \mu g A_0 + [ik_b^x \mu g \quad \hat{k}_b^x \mu g \quad 0] \mathbf{T}_r^{(i)} = [-ik_b \quad ik_b \quad -k_b \quad k_b \quad 0 \quad 0] \mathbf{T}^{(ii)}. \quad (18)$$

In the same way, by applying the continuous boundary condition of the longitudinal wave displacement at the interface, we get

$$[0 \quad 0 \quad \hat{\mu} \cdot \hat{g}] \mathbf{T}_r^{(i)} = [0 \quad 0 \quad 0 \quad 0 \quad 1 \quad 1] \mathbf{T}^{(ii)}, \quad (19)$$

where $\hat{g} = \text{sinc}(k_i^y \cdot p/2)$ and $\hat{\mu} = e^{-ik_i^y \cdot y_j}$.

By applying the continuous boundary condition of x -components of bending moment at the interface $x=0$, and integrating along y -direction in the region $y - y_j \leq |L/2|$, we can get

$$E_5 A_0 + [E_1 \ E_2 \ 0] \mathbf{T}_r^{(I)} = [-\varsigma_1 \ -\varsigma_1 \ \varsigma_1 \ \varsigma_1 \ 0 \ 0] \mathbf{T}^{(II)}, \quad (20)$$

where $E_1 = L \cdot [-(k_b^x)^2 - \nu(k_b^y)^2]$, $E_2 = L \cdot [(\hat{k}_b^x)^2 - \nu(k_b^y)^2]$, $\varsigma_1 = pk_b^2 g / \mu$, and $E_5 = L \cdot [-(k_b^x)^2 - \nu(k_b^y)^2]$. L and ν are the subunit period and Poisson's ratio, respectively. In the same way, by applying the continuous boundary condition of shear force at the interface, we can get

$$E_6 A_0 + [E_3 \ E_4 \ 0] \mathbf{T}_r^{(I)} = [i \cdot \varsigma_2 \ -i \cdot \varsigma_2 \ -\varsigma_2 \ \varsigma_2 \ 0 \ 0] \mathbf{T}^{(II)}, \quad (21)$$

where $E_3 = L \cdot [-i(k_b^x)^3 - (2-\nu)ik_b^x(k_b^y)^2]$, $E_6 = L \cdot [-i(k_b^x)^3 - (2-\nu)ik_b^x(k_b^y)^2]$, $\varsigma_2 = pk_b^3 g / \mu$, and $E_4 = L \cdot [(\hat{k}_b^x)^3 - (2-\nu)\hat{k}_b^x(k_b^y)^2]$. In the same way, by applying

the continuous boundary condition of axial force at the interface, we can get

$$\begin{bmatrix} 0 & 0 & Lk_l^x \end{bmatrix} \mathbf{T}_r^{(I)} = \begin{bmatrix} 0 & 0 & 0 & 0 & -pk_l \hat{\mu} \hat{g} & pk_l \hat{\mu} \hat{g} \end{bmatrix} \mathbf{T}^{(II)}. \quad (22)$$

According to Eq. (A7), we obtain the coefficient vector of the wavefield in the right interface of the pillared resonance

$$\mathbf{T}_R^{(P)} = N_1 \mathbf{T}_L^{(P)} = N_1 \mathbf{T}^{(II)}. \quad (23)$$

Since bending moment, shear force, and axial force are zero at the right free boundary of the waveguide resonant, and we can get

$$N_4 N_3 \mathbf{T}_R^{(P)} = N_4 N_3 N_1 \mathbf{T}^{(II)} = N_5 \mathbf{T}^{(II)} = 0, \quad (24)$$

where N_3 is the propagation matrix and expressed as

$$N_3 = \begin{bmatrix} e^{-ik_b s} & 0 & \dots & 0 \\ 0 & e^{ik_b s} & 0 & \vdots \\ & 0 & e^{-k_b s} & 0 \\ \vdots & & 0 & e^{k_b s} & 0 \\ & & & 0 & e^{-ik_l s} & 0 \\ 0 & \dots & & 0 & e^{ik_l s} \end{bmatrix}. \quad (25)$$

N_4 is the boundary state matrix and expressed as

$$N_4 = \begin{bmatrix} 0 & 0 & 0 & 0 & -i & i \\ -i & i & 1 & -1 & 0 & 0 \\ -1 & -1 & 1 & 1 & 0 & 0 \end{bmatrix}. \quad (26)$$

Eqs. (17)-(22) and Eq. (24), in turn, can be rewritten as

$$\begin{aligned} P_1 + \mathbf{H}_1 \mathbf{T}_r^{(I)} &= \mathbf{Q}_1 \mathbf{T}^{(II)} \\ P_2 + \mathbf{H}_2 \mathbf{T}_r^{(I)} &= \mathbf{Q}_2 \mathbf{T}^{(II)} \\ \mathbf{H}_3 \mathbf{T}_r^{(I)} &= \mathbf{Q}_3 \mathbf{T}^{(II)} \\ P_4 + \mathbf{H}_4 \mathbf{T}_r^{(I)} &= \mathbf{Q}_4 \mathbf{T}^{(II)}. \\ P_5 + \mathbf{H}_5 \mathbf{T}_r^{(I)} &= \mathbf{Q}_5 \mathbf{T}^{(II)} \\ \mathbf{H}_6 \mathbf{T}_r^{(I)} &= \mathbf{Q}_6 \mathbf{T}^{(II)} \\ \mathbf{Q}_7 \mathbf{T}^{(II)} &= 0 \end{aligned} \quad (27)$$

According to Eq. (27), we can get

$$\mathbf{G}_1 \cdot \begin{pmatrix} \mathbf{T}_r^{(I)} \\ \mathbf{T}^{(II)} \end{pmatrix} = \mathbf{G}_2, \quad (28)$$

where

$$\begin{aligned} \mathbf{G}_1 &= \begin{pmatrix} -\mathbf{H}_1^T & -\mathbf{H}_2^T & -\mathbf{H}_3^T & -\mathbf{H}_4^T & -\mathbf{H}_5^T & -\mathbf{H}_6^T & \mathbf{0} \\ \mathbf{Q}_1^T & \mathbf{Q}_2^T & \mathbf{Q}_3^T & \mathbf{Q}_4^T & \mathbf{Q}_5^T & \mathbf{Q}_6^T & \mathbf{Q}_7^T \end{pmatrix}^T, \\ \mathbf{G}_2 &= (P_1 \ P_2 \ 0 \ P_4 \ P_5 \ 0 \ 0 \ 0 \ 0)^T. \end{aligned}$$

Finally, according to Eq. (28), we can get the scattering equation of the whole resonator system

$$\begin{bmatrix} (R_b \ R_b^* \ R_{bl})^T \\ \mathbf{T}^{(II)} \end{bmatrix} = \mathbf{G}_1^{-1} \cdot \mathbf{G}_2 = \mathbf{M}_s, \quad (29)$$

R_b equals the first element of the column vector \mathbf{M}_s .

Based on Eq. (29), the dimensionless reflected energy coefficient $|R_b|^2$ of the vertically incident flexural wave, varying with the waveguide resonator length s/d and

frequency ω , is shown in Fig. 3(a). The scattering equation of the whole resonator system is the basis of the following theoretical study of elastic wave BIC, so it is necessary to verify its correctness by full-wavefield simulation. The simulated $|R_b|^2$ is shown in Fig. 3(b). Due to the high computational cost of simulation, we only used large step sizes for these variables of s/d and ω . However, we can still see that the overall trends of the results in Figs. 3(a) and 3(b) are the same. In addition, for a small range shown in the blue box in Fig. 3(b), these results are based on a fine variable grid and basically consistent with those in Fig. 3(a). For intuitively displaying the consistency, we chose the results at lines 1 and 2 in Fig. 3(b) to compare with that in Fig. 3(a), as shown in Fig. 3(c). According to Eqs. (29), (A24), and (A25), the total energy of all scattering modes $e_T = |R_b|^2 + \sqrt{3}|R_{bl}|^2/k_b d$ is calculated. It can be seen from Fig. 3(d) that the total energy e_T is unit, i.e., the power flow balance. The balance also verifies the correctness of the analytical model and indicates there is no other mode conversion, such as the SH wave, in our system.

2.4. Elastic BIC and elastic quasi-BIC physics

As shown in Fig. 3(a), the white dashed lines and green dotted lines, obtained by Eq. (2) and Eq.(10), correspond to the Fano resonance and destructive interference, respectively. Their intersections accurately predict the location of the vanishing linewidths, marked by the white circle. These vanishing linewidths are ideal local states with zero leakage in the continuous spectrum of radiating waves, i.e., the ideal BICs with infinite Q factor (Kodigala et al., 2017; Marinica et al., 2008).

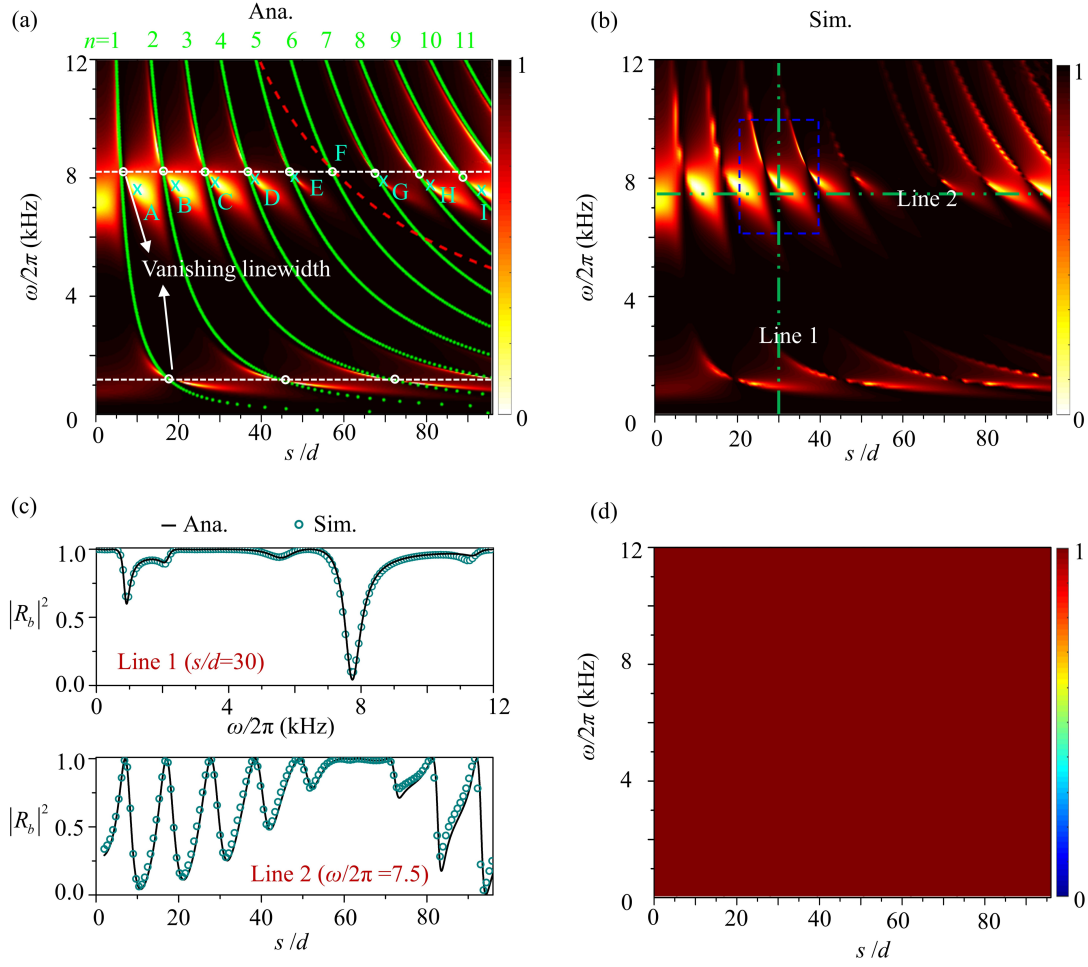


Fig. 3. (a) The analytical dimensionless reflected energy $|R_b|^2$ of the incident flexural wave in the whole resonant system, varying with frequency ω and the dimensionless waveguide length s/d . The green dotted lines and white dashed lines correspond to the destructive interference and Fano resonance, respectively. White circles and green crosses indicate the vanishing linewidths and trapped modes, respectively. (b) The simulated dimensionless reflected energy $|R_b|^2$ by using a large step for these variables of s/d and ω . In the blue box, these results are based on a fine variable grid. (c) Comparison between the analytical solutions and the simulated ones at lines 1 and 2 in (b). (d) The total dimensionless energy of all scattering modes in the whole resonance system.

These ideal BICs at the vanishing linewidths are entirely isolated and have no

access to the external radiation channel (Hsu et al., 2016; Huang et al., 2020). To get the TMPC, we need to tune the waveguide resonator length s to weaken the destructive interference described by Eq. (10). This weakening makes the resonance system leak small energy of the flexural wave (with radiative decay rate γ_b), which is radiating into the background plate. The leaked energy of the flexural wave will balance that of the longitudinal wave (with radiative decay rate γ_l) from the hybridization coupling of Fano resonance. This balance condition supporting trapped modes is $\gamma_b = \gamma_l$, equivalent to the so-called critical coupling (Cai et al., 2000), however here it is fulfilled by different mode conversion physics. The critical coupling can be demonstrated by the distribution of $\log_{10}|R_b|$ in the complex frequency plane, based on Eq. (29) (the detail see Appendix B). In this way, the incident flexural waves can be entirely trapped without any backscattering ($|R_b|^2 = 0$), i.e., tuning into the trapped mode (quasi-BIC). In addition, the system only allows the converted longitudinal waves to leak, leading to perfect mode conversion. Here, we only analyze these TMPCs near the second Fano resonance, which are marked from point A to point I [see discrete green crosses in Fig. 3(a)]. Among these points, the position deviation between point A and the adjacent vanishing linewidth is the largest. The reason is that the radiative energy of longitudinal wave around point A is the largest (explained in the next paragraph), which needs more weakening of the destructive interference to leak more flexural wave energy to balance. The more energy leakage leads to a wider reflection band.

For these marked TMPCs, the total radiative decay rate of the system $\gamma = \gamma_b + \gamma_l = 2\gamma_l$ corresponds to the Q factor of the system $Q = \bar{\omega}_0 / 2\gamma = \bar{\omega}_0 / 4\gamma_l$, where

$\bar{\omega}_0$ is about the second Fano resonance frequency. Therefore, γ_l decides the Q factor. The smaller the value of γ_l is, the greater the Q factor is. When one round-trip of the converted longitudinal wave between the right waveguide edge and the left one (the interface \tilde{l}) satisfies Fabry-Pérot resonance condition, γ_l approaches zero due to the resonance, which induces the TMPC with infinite Q factor. This Fabry-Pérot resonance condition is obtained by enforcing field relations at the waveguide resonator, and accordingly,

$$2sk_l = m\pi, \quad (30)$$

where m is a positive integer. According to Eq. (30), we can obtain Fabry-Pérot resonance frequency as $f_F = \sqrt{3}m/(2d\beta^2s)$. We calculate the first resonance frequency ($m = 1$) varying with waveguide lengths s , as shown by the red dashed line in Fig. 3(a). The red line approximately crosses over the vanishing linewidth near point F, which indicates that near the ideal local state, γ_l approaches zero due to the Fabry-Pérot resonance. Therefore, the flexural wave energy leakage from the trapped mode, balanced with the longitudinal wave energy leakage, also approaches zero. In this way, the position of TMPC almost overlaps with that of the ideal local state, approaching the BIC. At point F, the system with TMPC has a very narrow reflection band, which cannot be resolved in the scale of Fig. 3(a).

Based on R_b in the analytical model, we obtain the Q factor and γ of these TMPCs to quantitatively analyze the resonance characteristics (the detailed calculation can be found in Appendix C). It can be seen from Fig. 4(a) that the Q factor at point F exceeds 8000 (indeed approaches infinite-Q BIC). The closer to point F the other TMPC

is, the greater its Q factor is, and the lower its γ is. We chose two TMPCs with different radiative decay rates γ , corresponding to point A and point E in Fig.4(a), to calculate their dimensionless energy distributions of x -direction displacement in the unit structure by full wavefield simulations, as shown in the insets of Fig. 4(a). It can be clearly seen that the flexural wave energy is trapped at the top of the pillared resonator. In addition, for point E with a lower γ , the system captures more flexural wave energy (the multiple of the dimensionless energy enhancement arrives up to 282, relating to incident energy). The reason is that the lower γ is, the more trapped flexural wave energy in the resonance system with a higher Q is, which is similar to sound confinement from acoustic quasi-BIC (Huang et al., 2020). We note that by optimizing the parameters to satisfy Eqs. (2), (10), and (30) simultaneously, the Q of the system can be further increased. Therefore, our system can support the elastic BIC with an infinite Q. According to Eqs. (29), (A24), and (A25), we also show the curves of energy conversion ratio $\delta = \sqrt{3}|R_{bl}|^2/k_b d$ (see Appendix A) for these TMPCs (from point A to point F) to verify their perfect mode conversion, as shown in Fig. 4(b). All peak values of the curves approach one. For point F, the linewidth of the curve at its half-maximum is less than 1 Hz, which is consistent with its high Q.

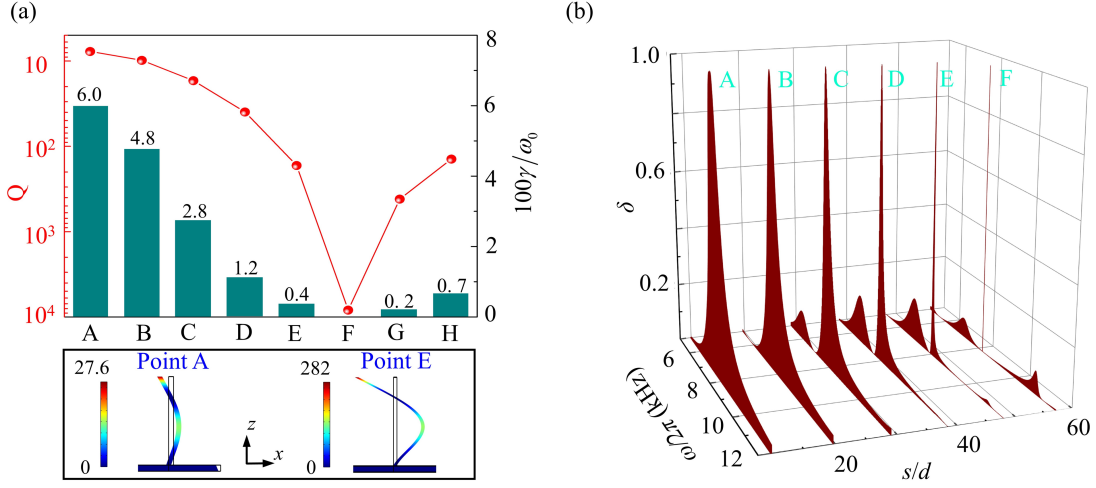


Fig. 4. (a) Bar charts represent total radiative decay rates γ of these TMPCs from point A to point H in Fig. 3(a). Red balls correspond to Q of these TMPCs. (b) Dimensionless energy conversion spectra $\delta = \sqrt{3}|R_{bl}|^2/k_b d$ for these TMPCs.

2.5. Transforming elastic quasi-BIC to elastic BIC

As shown above, for vertically incident wave, adjusting the Fabry-Pérot resonance of the waveguide resonator by changing the waveguide length s/d , we can change γ_l to obtain some discrete TMPCs with different Q, such as from point A to point I in Fig. 3(a). Further, for all these TMPCs (quasi-BIC), we can continuously tune them into the infinite-Q BIC by making their radiative decay rate close to zero, depending on tuning the critical frequency of mode conversion.

The critical frequency is decided by that the radiation angle θ_{bl}^r of the converted longitudinal wave equal to 90° . The radiation angle can be obtained as $\theta_{bl}^r = \arcsin(k_b \sin \theta^i / k_l)$ based on Snell's law. From the above equation, we get the critical frequency $f_c = 6 \sin^2 \theta^i / (\pi d^2 \beta^2)$, which is decided by the non-zero incident angle θ^i . When the frequency is lower than f_c , the calculated θ_{bl}^r is imaginary, that is,

the mode conversion disappears. For the TMPC marked by point B in Fig. 3(a), the dimensionless incident angle is changed as $\theta^i h/d = 77$, as an example. The interface impedance $Z_l = L / (p \cdot \cos \theta_{bl}^r)$ varying with frequency is shown in Fig. 5(a). At the critical frequency of $f_c = 8384$ Hz marked by the light blue dashed lines, Z_l is infinite, which will suppress longitudinal wave radiation. In addition, the corresponding $|R_b|^2$ for the obliquely incident flexural wave, calculated by Eq. (29), is shown in Fig. 5(b). The critical frequency closes to the Fano resonance frequency (marked by white dashed lines), the large Z_l reduces γ_l of the TMPC (marked by green crosses). The decreased $\gamma = 2\gamma_l$ leads to a narrower reflection band of the TMPC, compared with that of the TMPC marked by point B in Fig. 3(a).

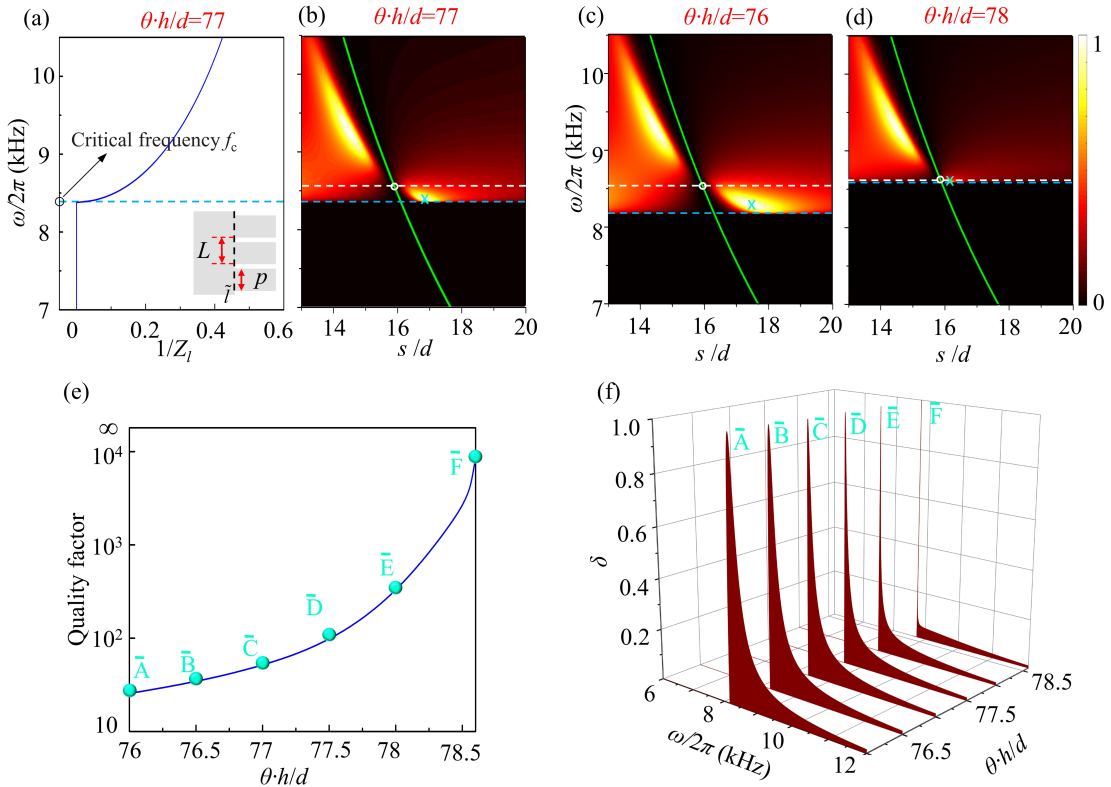


Fig. 5. (a) The interface impedance of the interface \tilde{l} for the converted longitudinal wave varying with frequencies. (b)-(d) The reflected flexural energy coefficients of the whole system, in the

frequency range from 7 kHz to 10.5 kHz and s/d range from 13 to 20, when the incident angles are $\theta h/d = 77$, $\theta h/d = 76$, and $\theta h/d = 78$, respectively. The light blue dashed lines indicate the critical frequency of 8384 Hz, 8169 Hz, and 8603 Hz. (e) Q of the trapped mode can be continuously changed with the incident angle. Q is over 8700 at point \bar{F} . (f) The dimensionless energy conversion spectra of the model at different incident angles. The linewidths of these curves at their half-maximum decrease from point \bar{A} to point \bar{F} .

Figs. 5(c) and 5(d) show $|R_b|^2$ for two other incident angles. Comparing Figs. 5(b)-5(d), the closer to the Fano resonance frequency the critical frequency is, the narrower the reflection band of the system with TMPC is. The Fano resonance frequencies have a slight increase, because the vertical wave vector changes with different incident angles. In addition, the position of TMPC [marked by green crosses in Figs. 5(b)-5(d)] is closer to the local states (marked by white circles), due to the low radiative decay rate. In this way, we can continuously change the critical frequency position to change the Q of the TMPC, as shown in Fig. 5(e), where the maximum Q is over 8700 at point \bar{F} . Fig. 5(f) shows peak values of dimensionless energy conversion spectra δ approach one for all TMPCs from point \bar{A} to point \bar{F} . The spectra linewidths at their half-maximum gradually decrease with approaching point \bar{F} . Theoretically, when the critical frequency intersects the Fano resonance frequency, TMPC coincides with the zero-linewidth ideal local state and supports an infinite-Q BIC.

3. Experimental evidence

In the experiment, we need to make great efforts to excite the ideal plane wave through the optimized array composed of several piezoelectric patches. To simplify the excitation, we simplify the model in Fig. 1(a) by a strip-like model (beam), as shown in the inset of Fig.6(a). Then, we can use a single piezoelectric patch attached on the strip-like model to excite the ideal incident wave, which significantly increases the accuracy of the experiment. We have proved that for vertically incident waves, the results of the simplified model are consistent with those of the original model by theoretical and simulation methods (see details in Appendix D). To confirm our theory, based on the simplified models, we print specimen one and specimen two with different waveguide lengths (10 and 29 mm) to verify different-Q-factor TMPCs based on quasi-BIC. These TMPCs correspond to point A and point C in Fig. 3(a).

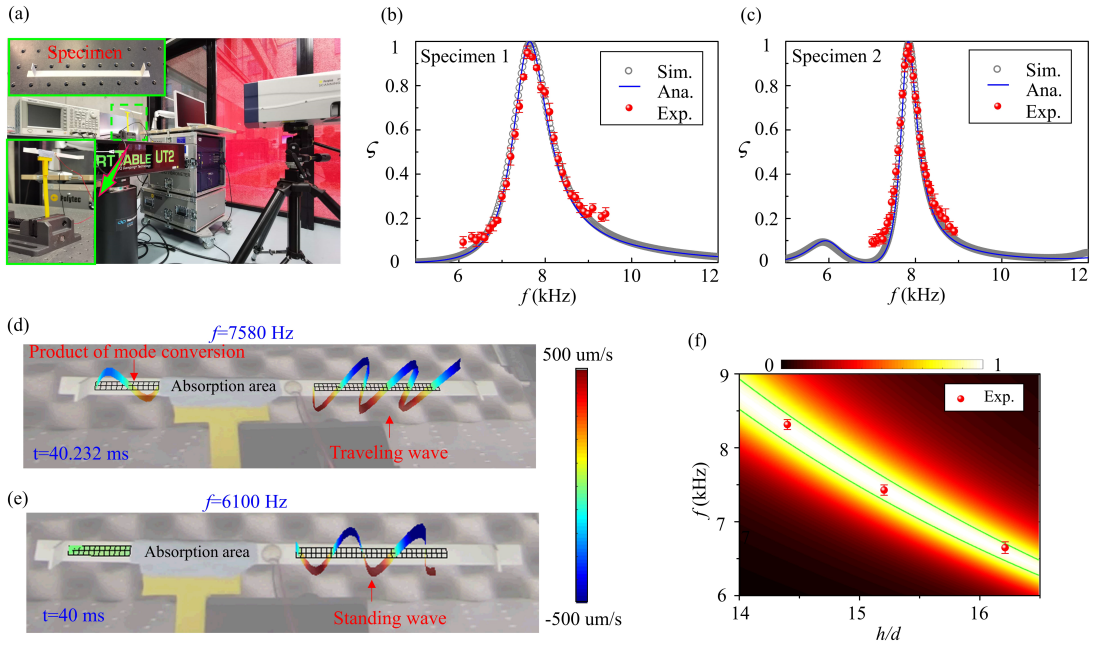


FIG. 6. (a) Experimental set-up. The specimen and the clamped test specimen are illustrated at the top and bottom. (b) and (c) The capture coefficients based on the measured velocity fields in two

specimens with waveguide lengths of 10 mm and 29 mm, respectively. Their heights h/d are 15. Theoretical and numerical results are also displayed for comparative verification. (d) The snapshots of Supplementary Video one in the central frequency of 7580 Hz. (e) The snapshots of Supplementary Video two in the central frequency of 6100 Hz. (f) Theoretical capture coefficients, varying the pillared resonator height h/d and frequency f . The waveguide resonator length is fixed as 10 mm. For three specimens with pillar heights h/d of 14.2, 15, and 16, the locations of measured trapped modes are around 8516.7 Hz, 7629 Hz, and 6848 Hz, respectively.

We use a Polytec scanning vibrometer (PSV-500) to measure the out-of-plane velocity field in these specimens. Then we obtain the capture coefficient ζ of flexural waves. The detailed experimental measurements can be found in Appendix E. To ensure the reliability of the data, we tested each experimental data three times. The experiment results with error bars for specimen one and specimen two are shown by red balls in Figs. 6(b) and 6(c), respectively. It can be seen that the peak values at 7580 Hz and 7850 Hz are approximately one, that is, the flexural waves are almost completely captured. A series of simulations using COMSOL Multiphysics has also been performed. These capture coefficient curves from the experiments and simulations have excellent agreements with that from the theory [solid lines in Figs. 6(b) and 6(c)]. Therefore, we confirm the existence of the trapped modes with different Q factors. Furthermore, based on the experimental data, we calculate that the converted energy ratios of longitudinal waves are more than 0.93 and 0.9 for peak points in Figs. 6(b) and 6(c), respectively, which confirm the perfect mode conversion of the trapped modes, neglecting small structural losses. The detailed calculation process can be seen in

Appendix G.

To intuitively show the TMPC, we obtain the dynamic full wavefield in specimen one at the central frequency of 7580 Hz by the “time” measurement mode of PSV 500. Fig. 6(d) shows a snapshot of Supplementary Video one at 40.232 ms. In the right test area, the wavefield is almost a traveling wave, as observed in the Supplementary Video 1. The existence of the traveling wave means flexural waves are completely captured by the right resonance system, that is, there is almost no reflection. The absorption area in the middle can completely absorb the flexural wave (relevant confirmation can be found in Appendix G), but we still clearly see the flexural wave field in the left test area. The abnormal phenomenon is caused by the mode conversion in the resonance system. For comparison, we test the dynamic full wavefield in specimen one at 6100 Hz (away from the central frequency). Figs. 6(e) shows a snapshot of Supplementary Video two. In the right test area, the incident wave is a standing wave. In the left test area, the amplitude of the flexural wave is close to zero, as observed in the Supplementary Video 2. The wave phenomenon in Supplementary Video two means that flexural waves are not captured by the right resonance system, and mode conversion does not happen either.

We note a subtle but essential difference between the TMPC in our system and the conventional trapped mode. The latter disappears when the parameters of the system slightly deviate from the designed structure, making it very difficult to observe experimentally (Hsu et al., 2013a; Hsu et al., 2016). In our theory, based on Eqs. (2) and (10), when the parameters of the system change, the vanishing linewidth jumps

from one frequency to another. Therefore, the TMPC near the vanishing linewidth shift their positions and do not disappear. For example, theoretical capture coefficients, varying the pillared resonator height h/d and frequency f , are shown in Fig. 6(f), when the waveguide length is fixed as 10 mm. The green lines are the contour lines of 0.9. High capture coefficients over a wide range indicate that the TMPCs are stable for various geometric parameters. Further, we have printed specimen three and specimen four with the same waveguide length of 10 mm. Their pillar heights h/d are 14.2 and 16. We can find the measured trapped modes ($\zeta \approx 1$) for specimens three and four at around 8516.7 Hz and 6848 Hz, respectively. These measured points are added to Fig. 6(f). It can be seen that these points are inside the contour line of 0.9, which are consistent with the theory results. The consistency confirms that the TMPCs are robust to changes in system parameters. Similar robustness of the trapped modes to system parameters can also be found in other BIC systems (Hsu et al., 2013a; Marinica et al., 2008).

4. Conclusions

We have theoretically predicted and experimentally demonstrated a TMPC in an elastic wave system. The system supports elastic BIC by achieving simultaneous hybrid Fano and Fabry-Pérot resonances. We prove that the TMPC supporting quasi-BIC can be tuned to the TMPC supporting infinite-Q BIC by bringing the critical frequency of mode conversion closer to the Fano resonance frequency. This work paves the way for the investigation of the intriguing physics related to the interaction between elastic

wave energies with different polarization planes, based on elastic BICs. The elastic BIC can obtain an unprecedented high quality factor in the elastic system, which may facilitate various applications, e.g., high-sensitivity elastic wave sensor and high-resolution elastic wave filters.

Acknowledgments

The authors acknowledge Professor Yong Li for fruitful discussions. This work is supported by the Air Force Office of Scientific Research under award number FA9550-18-1-7021, la Région Grand Est and Institut Carnot ICEEL. It is also supported by the National Natural Science Foundation of China (Grant No.11972296), the 111 Project (No. BP0719007), and the Fundamental Research Funds for the Central Universities (No. 310201901A005).

Appendix A. Analytical expression of the scattering coefficient for the pillared resonator

First, we consider an incident wave perpendicular to the model without the right boundary, as shown in Fig. 1(a). When the filling ratio of the slot $\hat{\eta}=(L-p)/L$ in the subunit is a small value ($\hat{\eta}=1/17$ in our study), the considered model is equivalent to the one without the slot. It is a one-dimensional model. The governing equations for the flexural wave and the longitudinal wave in the background plate can be expressed as the following forms, respectively:

$$\begin{aligned} \left(D \frac{\partial^4}{\partial x^4} + \rho d \frac{\partial^2}{\partial t^2} \right) w(x, t) &= 0 \\ \left(\frac{12}{\beta^4 d^2} \frac{\partial^2}{\partial x^2} - \frac{\partial^2}{\partial t^2} \right) u(x, t) &= 0 \end{aligned} \quad , \quad (\text{A1})$$

where ρ is the density of the background plate. D is the flexural rigidity,

$$D = \frac{Ed^3}{12(1-\nu^2)},$$

in which E , d , and ν are Young's modulus, plate thickness, and Poisson's ratio, respectively. β is the propagation constant, $\beta^4 = \rho d / D$.

The general solution of displacement for the fourth-order partial derivative governing equation of the flexural wave in the background plate is:

$$w(x, t) = \left(\tilde{A}e^{-ik_b x} + \tilde{B}e^{ik_b x} + \tilde{C}e^{-k_b x} + \tilde{D}e^{k_b x} \right) e^{i\omega t}, \quad (\text{A2})$$

where \tilde{A} , \tilde{B} , \tilde{C} , and \tilde{D} are complex coefficients. $\tilde{A}e^{-ik_b x}$ and $\tilde{B}e^{ik_b x}$ correspond to the positive-going and negative-going propagating flexural waves, whereas $\tilde{C}e^{-k_b x}$ and $\tilde{D}e^{k_b x}$ correspond to the positive-going and negative-going evanescent flexural waves. The flexural wavenumber is $k_b = \beta\sqrt{\omega}$, where $\omega = 2\pi f$ is the circular

frequency. The general solution of displacement for the second-order partial derivative governing equation of longitudinal waves in the background plate is:

$$u(x, t) = (\tilde{P}e^{-ik_l x} + \tilde{Q}e^{ik_l x})e^{i\omega t}, \quad (\text{A3})$$

where \tilde{P} and \tilde{Q} are complex coefficients. The longitudinal wavenumber k_l is $k_l = (\sqrt{3}/6)\beta^2 \omega d$.

Similarly, the general solutions of the displacements for the flexural wave and longitudinal wave equations in the pillared resonator are

$$\begin{cases} w^{(\text{P})}(z, t) = (A^{(\text{P})}e^{-i\tilde{k}_b z} + B^{(\text{P})}e^{i\tilde{k}_b z} + C^{(\text{P})}e^{-\tilde{k}_b z} + D^{(\text{P})}e^{\tilde{k}_b z})e^{i\omega t} \\ u^{(\text{P})}(z, t) = (P^{(\text{P})}e^{-i\tilde{k}_l z} + Q^{(\text{P})}e^{i\tilde{k}_l z})e^{i\omega t} \end{cases} \quad (\text{A4})$$

, respectively. The superscript (P) indicates the pillared resonator.

We make an incident positive-going flexural wave of $1 \cdot e^{i\omega t}$ at the left interface of the pillared resonator bottom, so the wave fields at the left interface (w_L, u_L) and the right interface (w_R, u_R) of the pillared resonator bottom can be expressed as follows:

$$\begin{cases} w_L(x, t) = (1 + r_b + r_{bb^*})e^{i\omega t} \\ u_L(x, t) = r_{bl}e^{i\omega t} \\ w_R(x, t) = (t_b + t_{bb^*})e^{i\omega t} \\ u_R(x, t) = t_{bl}e^{i\omega t} \end{cases}, \quad (\text{A5})$$

where the symbols t and r in t_b and r_b denote the transmission and reflection complex coefficients of the resonator, respectively. The subscript $*$ represents an evanescent flexural wave. The subscripts b and l represent the flexural mode (or bending wave) and longitudinal mode. The subscripts bl and lb represent the conversion from flexural wave to longitudinal wave and the reverse process, respectively. The

subscripts bb^* and b^*b represent the conversion from propagating flexural wave to evanescent one and the reverse process, respectively. Therefore, the vectors \mathbf{k}_L and \mathbf{k}_R for both sides of the bottom of the pillared resonator can be written as:

$$\begin{cases} \mathbf{k}_L = [1 & r_b & 0 & r_{bb^*} & 0 & r_{bl}]^T \\ \mathbf{k}_R = [t_b & 0 & t_{bb^*} & 0 & t_{bl} & 0]^T \end{cases} \quad (\text{A6})$$

The relationships between slope φ and the displacement w , between shear force V and the displacement w , between bending moment M and the displacement w , between axial force F and the displacement u are $\varphi = w'$, $V = -Dw''$, $M = Dw''$, and $F = 12\rho u' / (\beta^4 d^2)$, respectively. Among both side interfaces of the pillared resonator bottom, the boundary conditions of displacement, slope, bending moment, shear force, and axial force must be satisfied (Cao et al., 2021). According to these boundary conditions, we obtain the propagation equation:

$$\mathbf{k}_R = N_1 \mathbf{k}_L. \quad (\text{A7})$$

where N_1 is the transfer matrix.

From Eq. (A7), we can obtain

$$r_b = \frac{-8\Gamma_1 - 8\Gamma_1 \cdot \chi_1 - (4\Gamma_1 + 8\Gamma_2) \cdot \chi_2 + (4\Gamma_1 + 8\Gamma_2) \cdot \chi_3}{(4 - 4i) \cdot \chi_1 - 2i \cdot \chi_2 + 2i \cdot \chi_3 + 4 - 4i}, \quad (\text{A8})$$

$$t_b = \frac{-\delta_1 - \delta_1 \cdot \chi_1 - 4i\Gamma_4 \cdot \chi_2 + 4i\Gamma_4 \cdot \chi_3 + \Gamma_0}{(4 - 4i) \cdot (\chi_1 - 2i \cdot \chi_2 + 2i \cdot \chi_3 + 4 - 4i)}, \quad (\text{A9})$$

$$t_{bl} = r_{bl} = \frac{(2 - 2i)\kappa \cdot \chi_4}{(4 - 4i + \kappa) \cdot \chi_1 + (2\kappa + 2i\kappa - 2i) \cdot \chi_2 + (2i + 2\kappa + 2i\kappa) \cdot \chi_3 + 4 - 4i - \kappa}, \quad (\text{A10})$$

$$r_{bb^*} = \frac{\Gamma_3 [8i\chi_1 + (4 + 4i)\chi_2 - (4 + 4\kappa + 4i)\chi_3 + 8i] + \Gamma_4 (8\chi_2 - 8\chi_3)}{(1 - i) [8\chi_1 + (2 - 2i + 4i\kappa)\chi_2 - (2 - 2i - 4i\kappa)\chi_3 + 8]}, \quad (\text{11})$$

$$t_{bb^*} = \frac{-\Gamma_3 \left[(2-2i)\chi_1 + (a+ai)\chi_2 + (a+ai)\chi_3 + (4-4i) \right] - \Gamma_4 (2+2i)(\chi_2 - \chi_3)}{8\chi_1 + (2-2i)\chi_2 + (-2+2i+4ia)\chi_3 + 8}, \quad (12)$$

where $\delta_1 = 4i\Gamma_3 + 16i\Gamma_4$, $\kappa = \frac{k_l}{k_b}$, $\Gamma_0 = \frac{(2\kappa + 2i\kappa) \cdot \sin(k_b h) \cdot \cosh(k_b h)}{1 + (2\kappa - 2i\kappa) \cdot \cos(\kappa k_b h)}$,

$$\Gamma_1 = \frac{1}{2 + (4-4i)\kappa \cot(\kappa k_b h)}, \quad \Gamma_2 = \frac{1}{2 \tan(\kappa k_b h) / \kappa + (4-4i)},$$

$$\Gamma_3 = \frac{\sin(\kappa k_b h)}{\sin(\kappa k_b h) + \kappa(2-2i)\cos(\kappa k_b h)}, \quad \Gamma_4 = \frac{\kappa \cos(\kappa k_b h)}{\sin(\kappa k_b h) + \kappa(2-2i)\cos(\kappa k_b h)},$$

$$\chi_1 = \cos(k_b h) \cosh(k_b h), \quad \chi_2 = \cos(k_b h) \sinh(k_b h),$$

$$\chi_3 = \sin(k_b h) \cosh(k_b h), \quad \text{and} \quad \chi_4 = \sin(k_b h) \sinh(k_b h).$$

In the same way, we make an incident positive-going longitudinal wave of $1 \cdot e^{i\omega t}$ at the left interface of the pillared resonator bottom, so the wave fields at the left interface and the right interface of the pillared resonator bottom can be expressed as follows:

$$\begin{cases} \tilde{w}_L(x, t) = (r_{lb} + r_{lb^*}) e^{i\omega t} \\ \tilde{u}_L(x, t) = (1 + r_l) \cdot e^{i\omega t} \\ \tilde{w}_R(x, t) = (t_{lb} + t_{lb^*}) e^{i\omega t} \\ \tilde{u}_R(x, t) = t_l e^{i\omega t} \end{cases}, \quad (A13)$$

The vectors \mathbf{k}_L and \mathbf{k}_R for both sides of the pillared resonator bottom can be rewritten as:

$$\begin{cases} \mathbf{k}_L = [0 \quad r_{lb} \quad 0 \quad r_{lb^*} \quad 1 \quad r_l]^T \\ \mathbf{k}_R = [t_{lb} \quad 0 \quad t_{lb^*} \quad 0 \quad t_l \quad 0]^T \end{cases}. \quad (A14)$$

According to Eq. (A7), we can obtain

$$r_l = \frac{-\kappa\chi_1 - (2\kappa + 2\kappa i)\chi_3 - (2\kappa + 2\kappa i)\chi_2 + \kappa}{(4 + \kappa - 4i)\chi_1 + (2\kappa + 2\kappa i - 2i)\chi_2 + (2\kappa + 2i + 2\kappa i)\chi_3 + 4 - 4i - \kappa}, \quad (A15)$$

$$t_l = \frac{(4-4i)\chi_1 - 2i\chi_2 + 2i\chi_3 + 4-4i}{(4-4i+\kappa)\chi_1 + (2\kappa+2\kappa i-2i)\chi_2 + (2i+2\kappa+2\kappa i)\chi_3 + 4-4i-\kappa}, \quad (\text{A16})$$

$$r_{lb} = -t_{lb} = \frac{2\chi_4}{(8+\kappa+\kappa i)\chi_1 + (2-2i+4\kappa i)\chi_2 + (-2+2i+4\kappa i)\chi_3 + 8-\kappa-\kappa i}, \quad (\text{A17})$$

$$r_{lb}^* = \frac{(1+i)\chi_4}{-(4+4i)\chi_1 + (2a-2-2ai)\chi_2 + (2a+2-2ai)\chi_3 - 4-4i}, \quad (\text{A18})$$

$$t_{lb}^* = \frac{2\chi_4}{8\chi_1 + (2+4ai-2i)\chi_2 + (-2+2i+4ai)\chi_3 + 8}. \quad (\text{A19})$$

In the same way, we make an incident evanescent flexural wave of $1 \cdot e^{i\omega t}$ at the left interface of the pillared resonator bottom, and we can obtain the coefficients of r_b^* ,

t_{b^*} , r_{b^*b} , t_{b^*b} , r_{b^*l} , and t_{b^*l} .

As shown in Fig. 1(b), the single pillared resonance hybridizes the input flexural waves (b_{1+} , b_{2+}), input longitudinal waves (l_{1+} , l_{2+}), output flexural waves (b_{1-} , b_{2-}), and output longitudinal waves (l_{1-} , l_{2-}). Therefore, we can obtain the scattering equation of the pillared resonator in the far-field:

$$\mathbf{S}^- = \begin{bmatrix} t_b & r_b & t_{lb} & -r_{lb} \\ r_b & t_b & r_{lb} & -t_{lb} \\ t_{bl} & -r_{bl} & t_l & r_l \\ r_{bl} & -t_{bl} & r_l & t_l \end{bmatrix} \mathbf{S}^+ = \mathbf{M}_P \cdot \mathbf{S}^+, \quad (\text{A20})$$

where $\mathbf{S}^- = [b_{2-}, b_{1-}, l_{2-}, l_{1-}]^T$ and $\mathbf{S}^+ = [b_{1+}, b_{2+}, l_{1+}, l_{2+}]^T$. \mathbf{M}_P is the scattering matrix.

We note that the scattering matrix can also be derived directly from the transfer matrix.

The negative sign in Eq. (A20) is to make the scattering matrix and transfer matrix

keep consistent in mathematical form.

Based on the analytical model, we can analyze its band structure to intuitively show the hybridization coupling between flexural waves and longitudinal waves from the Fano resonance. The unit structure is shown in the illustration of Fig. 2(c). \hat{D} is a

typical period with a quarter wavelength in the second Fano resonance frequency. Due to the subwavelength period, the evanescent flexural modes need to be considered in the scattering matrix, \mathbf{M}_p will be rewritten as

$$\tilde{\mathbf{M}}_p = \begin{bmatrix} t_b & r_b & t_{b^*b} & r_{b^*b} & t_{lb} & -r_{lb} \\ r_b & t_b & r_{b^*b} & t_{b^*b} & r_{lb} & -t_{lb} \\ t_{bb^*} & r_{bb^*} & t_{b^*b^*} & r_{b^*b^*} & t_{lb^*} & -r_{lb^*} \\ r_{bb^*} & t_{bb^*} & r_{b^*b^*} & t_{b^*b^*} & r_{lb^*} & -t_{lb^*} \\ t_{bl} & -r_{bl} & t_{b^*l} & -r_{b^*l} & t_l & r_l \\ r_{bl} & -t_{bl} & r_{b^*l} & -t_{b^*l} & r_l & t_l \end{bmatrix}. \quad (\text{A21})$$

Therefore, the scattering matrix including the phase origins (Botten et al., 2001) and evanescent flexural modes can be obtained as

$$\mathbf{M}_p^* = \Upsilon \tilde{\mathbf{M}}_p \Upsilon, \quad (\text{A22})$$

where

$$\Upsilon = \begin{bmatrix} e^{-ik_b \hat{D}/2} & & & & & \\ & e^{-ik_b \hat{D}/2} & & & & \\ & & e^{-k_b \hat{D}/2} & & & \\ & & & e^{-k_b \hat{D}/2} & & \\ & & & & e^{-k_l \hat{D}/2} & \\ & & & & & e^{-k_l \hat{D}/2} \end{bmatrix}. \quad (\text{A23})$$

For the flexural wave with the amplitude of \bar{A}_b , its energy can be expressed as

$$e_b = \omega D k_b^3 |\bar{A}_b|^2. \quad (\text{A24})$$

For the longitudinal wave with the amplitude of \bar{A}_l , its energy can be expressed as

$$e_l = 6\omega D k_l |\bar{A}_l|^2 / d^2. \quad (\text{A25})$$

For the incident flexural wave of $1 \cdot e^{i\omega t}$, the dimensionless energy of the reflected and transmitted flexural waves can be expressed as $e_{r_b} = |r_b|^2$ and $e_{t_b} = |t_b|^2$, respectively.

According to Eqs. (A24) and (A25), the dimensionless energy of the reflected and

transmitted longitudinal waves from the mode conversion can be expressed as $e_{r_{bl}} = \sqrt{3}|r_{bl}|^2/k_b d$ and $e_{t_{bl}} = \sqrt{3}|t_{bl}|^2/k_b d$, respectively. The total scattering energy can be expressed as $e_t = e_{r_b} + e_{t_b} + e_{r_{bl}} + e_{t_{bl}}$.

Appendix B. The critical coupling of TMPC

We employ the complex frequency plane to analyze the capture features and manifest their distinct coupling characteristics qualitatively. By replacing the frequency as $f' = \text{Real}(f') + \text{Imag}(f')$, the reflection/capture properties of an elastic system are described by the real frequency $\text{Real}(f')$ and the imaginary frequency $\text{Imag}(f')$ in a complex frequency plane. After substituting f' into the scattering equation Eq. (29) of the elastic system, the reflection coefficient R_b becomes a function of both real frequency $\text{Real}(f')$ and imaginary frequency $\text{Imag}(f')$. Then in a complex frequency plane, a colormap illustrating the distribution of $\log_{10}|R_b|$ can be plotted, as shown in Fig. 7(a). “Zero” and “Pole” are two extreme points referring to the lowest and the highest values of the reflection coefficient.

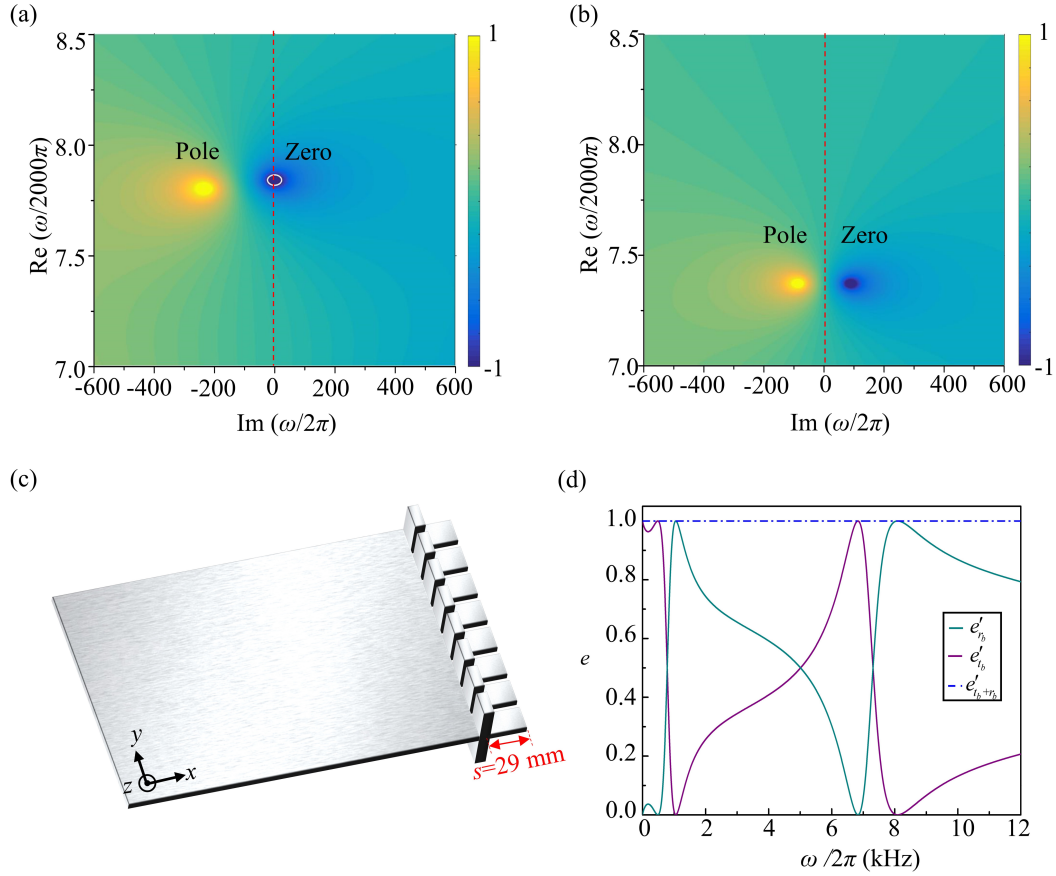


Fig. 7. (a) The complex frequency graphs illustrating the distribution of $\log_{10}|R_b|$ in the complex frequency plane, corresponding to the system with TMPC marked by point C in Fig. 3(a). (b) The corresponding complex frequency graph for the symmetrical model in (c). (c) Symmetrical double pillared resonators in a semi-infinite plate. The waveguide length s is 29 mm. (d) The dimensionless energy curves of reflected flexural wave E_{r_b} and transmitted flexural wave E_{t_b} . The total energy $E_{t_b+r_b}$ is also shown by the blue dotted line.

For comparison, we analyze symmetrical double pillared resonators in a semi-infinite plate, as shown in Fig. 7(c). The boundary condition of the symmetrical double pillared resonators is modified according to the structural symmetry. First, for infinite plate without right boundary, we obtain the analytical expression of the scattering

coefficient, based on the similar method of Appendix A. Fig. 7(d) displays the dimensionless energy curves of reflected and transmitted flexural waves. The total energy is unit [marked by the blue dotted line in Fig. 7(d)], which indicates that there is only the flexural wave in the system, and there is no longitudinal wave produced by hybrid coupling. The reason is that the shear force generated by the upper and lower symmetrical pillared resonator is balanced, which leads to the decoupling of the longitudinal axial force in the background plate and the shear force in the pillared resonator. Then, considering the introduction of the right waveguide resonator with the length s , we get the scattering equation of the resonator system. Fig. 7(b) shows the corresponding complex frequency graph. “Zero” and “Pole” points are always symmetrical about the real frequency axis. The reflection coefficient of the flexural wave is equal to 1 in the whole frequency range.

When the resonant structure of the system is a side-coupled pillared resonator in Fig. 1(a), the hybrid coupling will induce the mode conversion to leak longitudinal wave. The leakage energy of the flexural wave is similar to dissipative loss in the optical resonance system. But the “dissipative loss” is from the hybridization coupling in our study. Fig. 7(a) shows the complex frequency graphs, corresponding to the system with TMPC marked by point C in Fig. 3(a). “Zero” point and “Pole” point have shifted to the left, and “Zero” point intersects the real frequency axis. The intersection is the so-called critical coupling, however here it is fulfilled by different mode conversion physics. The flexural wave is completely trapped by the system. For the critical coupling (Cai et al., 2000), the energy leakage of the flexural wave γ_b will balance

that of the longitudinal wave γ_l from hybridization coupling of Fano resonance.

Appendix C. Q factor and γ of these TMPCs

Since the energy leaks out from the resonator, each TMPC can be characterized by “Pole” point in the complex frequency graphs, as shown in Figs. 7(a) and 7(b). The frequency of the Pole is $f_{\text{Pole}} = \text{Real}(f_{\text{Pole}}) + i \cdot \text{Imag}(f_{\text{Pole}})$, with the position at the real axis $\text{Real}(f_{\text{Pole}})$. The TMPC has the decay rate $\gamma = -\text{Imag}(f_{\text{Pole}})$ (Krasnok et al., 2019), which determines the linewidth of TMPC at its half-maximum. The Pole is close to the real frequency axis, the Q of the TMPC can be defined as

$$Q = \frac{-\text{Real}(f_{\text{Pole}})}{2 \cdot \text{Imag}(f_{\text{Pole}})}, \quad (\text{C1})$$

In our system, the decay rate γ includes both flexural wave radiative γ_b and converted longitudinal wave radiative (similar to dissipation) γ_l (Bliokh et al., 2008).

In Fig. 5(f), for the TMPCs with a steep rise from 0 to 1, their Q factor can be calculated by $Q = f_c / \Delta f$, where f_c is the central frequency of the resonance peak, and Δf is the full width at half maximum for the peak.

Appendix D. Simplified specimens and their manufacture

For the theoretical model in Fig. 1(a), the filling ratio of a slot $(L-p)/L$ in a subunit is a small value of 1/17, and the periodic L is 85 mm. When considering an incident wave perpendicular to the model, we can simplify the two-dimensional (2D) periodic structure to a one-dimensional (1D) strip-like model shown in Fig. 8(a). The

theory and simulated results show that the capture coefficients of the flexural waves for the 1D simplified models and the 2D ones are consistent, as shown in Figs. 8(b) and 8(c). We can print specimens to verify supporting the trapped modes corresponding to point A and point C in Fig. 3(a). The 3D-printer Ultimaker 3, with a manufacturing precision of 0.06 mm, is adopted. The corresponding geometric parameters of the two specimens are shown in TABLE 1. The left pillared resonator and the right one are symmetrical about the specimen center. The purpose of designing the left resonator is to reconvert the longitudinal wave into the flexural wave, which will be described in detail later.

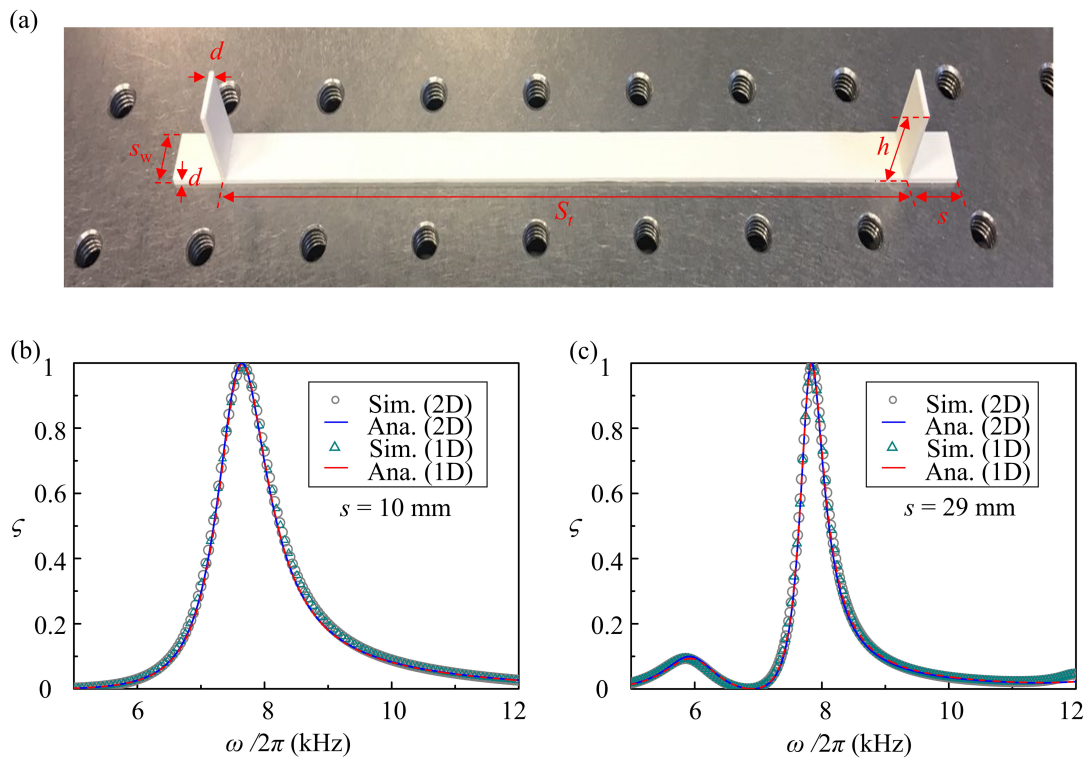


Fig. 8. (a) 1D simplified specimen marked by geometric parameter symbol. (b) The analytical and simulated capture coefficients of flexural waves in the 1D simplified model with $s = 10$ mm and the corresponding 2D one, respectively. (c) The analytical and simulated capture coefficients of flexural waves in the 1D simplified model with $s = 29$ mm and the corresponding 2D one, respectively.

TABLE 1. The geometric parameters of the specimen. All parameters are in units of mm.

d	h	s_w	s_t	s (Specimen 1)	s (Specimen 2)
1	15	8	160	10	29

Appendix E. Experimental set-up and measurements

As shown in Fig. 9, a 6-mm-diameter circular PZT patch, with a distance of $53d$ from the right pillared resonator, is bonded on the plate surface. The PZT patch is driven by a signal generator (Tektronix AFG3022C). The blue-tack layer is bonded in the middle of the strip-like specimen to absorb the left propagating flexural wave excited by the PZT patch and the reflected flexural wave from the right resonance structures. The left pillared and waveguide resonators can reconvert all the longitudinal waves, which are from the mode conversion in the right resonators, into flexural waves due to wave reciprocity. Then the reconverted flexural waves propagating to the right are absorbed by the middle blue-tack. In this way, the blue-tack can be equivalent to a non-reflection boundary of flexural waves.

The specimen surface is held perpendicular to the laser beam from PSV-500 scanning laser Doppler vibrometer, through a C-clamp and supporting rod applied to the lower edge, as shown in Fig. 9. The PSV-500 scanning head records the out-of-plane complex velocity in point 1 and point 2, marked in Fig. 9. The distance between the two points is less than an eighth wavelength. Simultaneously, their locations and the boundary of the resonance structure meet the far-field assumption (Cao et al., 2020). The assumption ensures that the measurement wavefield of the two points can

approximate the sum of incident and reflection propagating waves. An ensemble average with 20 samples is used at every measurement point to ensure the signal quality.

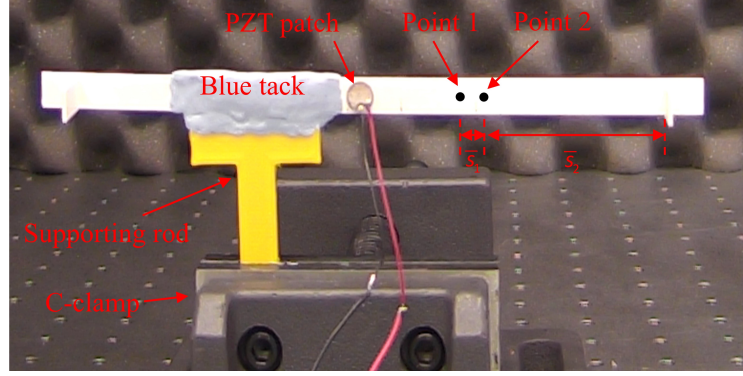


Fig. 9. Test set-up.

Using the measurement mode “FFT” of PSV-500, the complex velocities of flexural waves in points 1 and 2 can be measured and marked as v^1 and v^2 , respectively. They are expressed as $v^1 = V_1 \cdot e^{i(\bar{s}_1 + \bar{s}_2) \cdot \hat{k}_b} + V_R \cdot e^{-i(\bar{s}_1 + \bar{s}_2) \cdot \hat{k}_b}$ and $v^2 = V_1 e^{i\bar{s}_2 \cdot \hat{k}_b} + V_R e^{-i\bar{s}_2 \cdot \hat{k}_b}$, respectively. \bar{s}_1 and \bar{s}_2 are the distance marked in Fig. 9. \hat{k}_b is the flexural wave number. The transfer function H_{12} of the total wavefield in the two points can be obtained from the measured complex velocities of v^1 and v^2 . It can be expressed as $H_{12} = v^2/v^1 = \left(e^{i\hat{k}_b \bar{s}_2} + \tilde{r} e^{-i\hat{k}_b \bar{s}_2} \right) / \left[e^{i\hat{k}_b (\bar{s}_1 + \bar{s}_2)} + \tilde{r} e^{-i\hat{k}_b (\bar{s}_1 + \bar{s}_2)} \right]$, where the reflection coefficient $\tilde{r} = V_R / V_1$. Then, we can calculate the reflection coefficient of flexural waves as

$$\tilde{r} = \left(H_{12} - e^{-i\hat{k}_b \bar{s}_1} \right) \cdot e^{i2(\bar{s}_1 + \bar{s}_2) \cdot \hat{k}_b} / \left(e^{-i\hat{k}_b \bar{s}_1} - H_{12} \right). \quad (E1)$$

The reflection spectra of flexural wave energy can be obtained by $|\tilde{r}|^2$. The amplitude of the longitudinal wave cannot be measured directly by the single scanning head of our PSV-500. But we can measure the capture coefficient of $\zeta = 1 - |\tilde{r}|^2$ to characterize the energy capture of the flexural wave for the trapped modes.

Appendix F. Material parameter test of 3D-printed specimens

We note that the wavenumber \hat{k}_b in Eq. (E1) needs to be calculated by material parameters of 3D-printed specimens. All theories are also based on these material parameters. In the following, we will test the parameters. Although related material parameters of PLA, adopt in our 3D printer, have been reported in some literature. However, the material properties of practical printed specimens could be different due to various printing processes. To make the experiment and theory result more matching, we set the fixed printing mode, for example, infill density and infill pattern, to print all specimens. Then we print a beam specimen (180 mm × 8 mm × 1 mm) without pillared resonators. We first measure the mass and volume of the beam specimen to obtain its density of $\rho = 1086.3 \text{ kg/m}^3$. The blue-tacks are attached to the left and right ends of the beam specimen to eliminate the boundary reflection. We measure the flexural wavelength for ten test cases with different frequencies by the full wavefield test of PSV-500 in the frequency domain. From $k_b = \beta\sqrt{\omega}$, we can get

$$E = \varepsilon\omega^2\lambda_b^4, \quad (\text{F1})$$

where $\varepsilon = 3\rho(1-\nu^2)/(4\pi^4d^2)$ and $\nu = 0.35$. λ_b is the measured flexural wave wavelength. According to Eq. (F1), we calculate all Young's modulus for ten test cases.

Then we get the average of the calculated Young's modulus is $3.44 \times 10^9 \text{ Pa}$.

Appendix G. Verification of the perfect mode conversion

It can be seen from the experimental curve in Fig. 6(b) that the capture coefficient

of flexural wave in specimen 1 approaches the max value in the 7580 Hz. Below, as an example, we experimentally verify the perfect mode conversion in the trapped mode. First, we put blue-tacks on the left and right ends of specimen 1 to eliminate any reflection and mode conversion, as shown in Fig. 10(a). We measure the dimensionless amplitude of the flexural wave in point 3 as almost zero, which confirms the blue-tack in the middle can completely absorb the left propagating flexural wave excited by the PZT patch.

If we remove the blue-tacks on the left and right ends, there will be the longitudinal wave from the mode conversion in the right resonant system (defined as the first mode conversion), as shown in Fig. 10(b). Due to a large longitudinal wavelength, the blue-tack in the middle can absorb only part of the longitudinal wave. The unabsorbed longitudinal wave passes through the blue-tack onto the left side. Then the longitudinal wave is completely reconverted to a flexural wave in the left resonant system (defined as the second mode conversion) due to wave reciprocity. We measure the dimensionless amplitude of the flexural wave in point 5 is 0.48. Due to energy conservation, the unabsorbed longitudinal wave's energy is $E_1^l=0.48^2$. We can compensate the absorbed longitudinal wave's energy to E_1^l to obtain the total longitudinal wave's energy from the first mode conversion.

In Fig. 10(b), we consider the middle area attached blue-tack as an effective one, i.e., isotropic plate. Due to the loss in blue-tack, the wavenumbers of flexural wave and longitudinal wave in the effective area are induced into the imaginary part, i.e., $k_{\text{eff}}^b = \text{Re}(k_{\text{eff}}^b) - \text{Im}(k_{\text{eff}}^b) \cdot i$ and $k_{\text{eff}}^l = \text{Re}(k_{\text{eff}}^l) - \text{Im}(k_{\text{eff}}^l) \cdot i$. According to $k_b = \beta\sqrt{\omega}$

and $k_l = (\sqrt{3}/6)\beta^2 \omega d$, we obtain

$$\frac{k_{\text{eff}}^l}{(k_{\text{eff}}^b)^2} = \frac{d_{\text{eff}}}{\sqrt{12}} > \frac{d}{\sqrt{12}}. \quad (\text{G1})$$

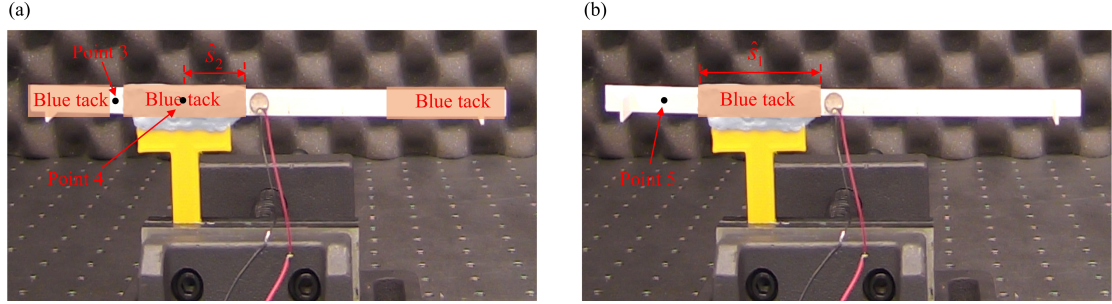


Fig. 10. (a) Specimen 1 with blue-tacks on the middle, the left end, and the right end. (b) Specimen 1 without blue-tacks on the left and right ends.

Then, we measure the dimensionless amplitude of the flexural wave in point 4 as 0.36. We only consider the loss in the blue-tack.

$$\mathcal{G}_1 = \left| e^{-\text{Im}(k_{\text{eff}}^b)\hat{s}_2} \right|^2 = 0.36^2. \quad (\text{G2})$$

According to Eqs. (G1) and (G2), we obtain the energy dissipation rate of the longitudinal wave from the PZT patch to point 3

$$\mathcal{G}_2 = \left| e^{-\text{Im}(k_{\text{eff}}^l)\hat{s}_1} \right|^2 = \left| e^{-\frac{d_{\text{eff}} \text{Re}(k_{\text{eff}}^b) \text{Im}(k_{\text{eff}}^b)}{\sqrt{3}} \hat{s}_1} \right|^2 > \mathcal{G}_1 \frac{1}{\sqrt{3}} \text{Re}(k_{\text{eff}}^b) \tilde{m} d. \quad (\text{G3})$$

where $\text{Re}(k_{\text{eff}}^b) \approx k_b|_{f=7580 \text{ Hz}}$, $\hat{s}_1 = \tilde{m}\hat{s}_2$ and $\tilde{m}=2$. Therefore, we can get the total energy of the longitudinal wave from the first mode conversion is

$$E_t^l = \frac{E_1^l}{\mathcal{G}_2}. \quad (\text{G4})$$

According to Eqs. (G3) and (G4), after compensating the energy absorbed by the blue-tack, the total energy of the converted longitudinal wave is $E_t^l > 0.93$. The high longitudinal wave's energy verifies the perfect mode conversion. The reason that the

value of E_t^l is less than 1 is existing small loss.

Appendix H: Simulation method

All simulations are performed in “Solid Mechanics Module” of COMSOL Multiphysics 5.5 software. The simulated results in Fig. 2(a), Fig. 3, and Fig. 6 are obtained by the “Frequency Domain” study. PMLs are used on all outer boundaries to avoid any reflections from the boundaries. The reflection coefficients are calculated by Eq. (E1) in the post-processing of the software. The simulated band structure in Fig. 2(b) is solved by the “Eigenfrequency” study.

References

- Bliokh, K.Y., Bliokh, Y.P., Freilikher, V., Savel'ev, S., Nori, F., 2008. Colloquium: Unusual resonators: Plasmonics, metamaterials, and random media. *Rev Mod Phys* 80, 1201-1213.
- Botten, L.C., Nicorovici, N.A., McPhedran, R.C., Sterke, C.M., Asatryan, A.A., 2001. Photonic band structure calculations using scattering matrices. *Phys Rev E Stat Nonlin Soft Matter Phys* 64, 046603.
- Cai, M., Painter, O., Vahala, K.J., 2000. Observation of Critical Coupling in a Fiber Taper to a Silica-Microsphere Whispering-Gallery Mode System. *Phys Rev Lett* 85, 74-77.
- Callan, M., Linton, C.M., Evans, D.V., 1991. Trapped modes in two-dimensional waveguides. *J Fluid Mech* 229, 51-64.
- Cao, L., Yang, Z., Xu, Y., Chen, Z., Zhu, Y., Fan, S.-W., Donda, K., Vincent, B., Assouar, B., 2021. Pillared elastic metasurface with constructive interference for flexural wave manipulation. *Mech Syst Signal Pr* 146, 107035.
- Cao, L., Yang, Z., Xu, Y., Fan, S.-W., Zhu, Y., Chen, Z., Li, Y., Assouar, B., 2020. Flexural wave absorption by lossy gradient elastic metasurface. *J Mech Phys Solids* 143, 104052.
- Cobelli, P.J., Pagneux, V., Maurel, A., Petitjeans, P., 2011. Experimental study on water-wave trapped modes. *J Fluid Mech* 666, 445-476.
- Colombi, A., Colquitt, D., Roux, P., Guenneau, S., Craster, R.V., 2016a. A seismic metamaterial: The resonant metawedge. *Sci Rep* 6, 27717.
- Colombi, A., Roux, P., Guenneau, S., Gueguen, P., Craster, R.V., 2016b. Forests as a natural seismic metamaterial: Rayleigh wave bandgaps induced by local resonances. *Sci Rep* 6, 19238.
- Colquitt, D.J., Colombi, A., Craster, R.V., Roux, P., Guenneau, S.R.L., 2017. Seismic metasurfaces: Sub-wavelength resonators and Rayleigh wave interaction. *J Mech Phys Solids* 99, 379-393.
- Cumpsty, N.A., Whitehead, D.S., 1971. The excitation of acoustic resonances by vortex shedding. *J Sound Vib* 18, 353-369.
- Doskolovich, L.L., Bezus, E.A., Bykov, D.A., 2019. Integrated flat-top reflection filters operating near bound states in the continuum. *Photonics Research* 7, 1314.
- Fan, S., Suh, W., Joannopoulos, J.D., 2003. Temporal coupled-mode theory for the Fano resonance in optical resonators. *Journal of the Optical Society of America A* 20, 569-572.
- Fano, U., 1961. Effects of Configuration Interaction on Intensities and Phase Shifts. *Phys Rev* 124, 1866-1878.
- Foley, J.M., Young, S.M., Phillips, J.D., 2014. Symmetry-protected mode coupling near normal incidence for narrow-band transmission filtering in a dielectric grating. *Phys Rev B* 89, 165111.
- Giurgiutiu, V., 2007. Structural health monitoring with piezoelectric wafer active sensors.
- Graff, K.F., 1975. Wave motion in elastic solids.
- Haq, O., Shabanov, S., 2021. Bound States in the Continuum in Elasticity. *Wave Motion* 103.
- Hirose, K., Liang, Y., Kurosaka, Y., Watanabe, A., Sugiyama, T., Noda, S., 2014. Watt-class high-power, high-beam-quality photonic-crystal lasers. *Nat Photonics* 8, 406-411.
- Hsu, C.W., Zhen, B., Chua, S.-L., Johnson, S.G., Joannopoulos, J.D., Soljačić, M., 2013a. Bloch surface eigenstates within the radiation continuum. *Light: Science & Applications* 2, e84-e84.
- Hsu, C.W., Zhen, B., Lee, J., Chua, S.-L., Johnson, S.G., Joannopoulos, J.D., Soljačić, M., 2013b. Observation of trapped light within the radiation continuum. *Nature* 499, 188-191.
- Hsu, C.W., Zhen, B., Stone, A.D., Joannopoulos, J.D., Soljačić, M., 2016. Bound states in the continuum.

Nat. Rev. Mater. 1.

Huang, S., Liu, T., Zhou, Z., Wang, X., Zhu, J., Li, Y., 2020. Extreme Sound Confinement From Quasibound States in the Continuum. *Phys Rev Appl* 14.

Imada, M., Noda, S., Chutinan, A., Tokuda, T., Murata, M., Sasaki, G., 1999. Coherent two-dimensional lasing action in surface-emitting laser with triangular-lattice photonic crystal structure. *Appl Phys Lett* 75, 316-318.

Ju, C.-Y., Chou, M.-H., Chen, G.-Y., Chen, Y.-N., 2020. Optical quantum frequency filter based on generalized eigenstates. *Opt Express* 28, 17868-17880.

Kawachi, O., Mineyoshi, S., Endoh, G., Ueda, M., Ikata, O., Hashimoto, E., Yamaguchi, M., 2001. Optimal cut for leaky SAW on LiTaO₃ for high performance resonators and filters. *IEEE Transactions on Ultrasonics, Ferroelectrics, and Frequency Control* 48, 1442-1448.

Kodigala, A., Lepetit, T., Gu, Q., Bahari, B., Fainman, Y., Kanté, B., 2017. Lasing action from photonic bound states in continuum. *Nature* 541, 196-199.

Koshelev, K., Bogdanov, A., Kivshar, Y., 2019. Meta-optics and bound states in the continuum. *Sci Bull* 64, 836-842.

Krasnok, A., Baranov, D., Li, H., Miri, M.-A., Monticone, F., Alú, A., 2019. Anomalies in light scattering. *Advances in Optics and Photonics* 11.

Kweun, J.M., Lee, H.J., Oh, J.H., Seung, H.M., Kim, Y.Y., 2017. Transmodal Fabry-Perot Resonance: Theory and Realization with Elastic Metamaterials. *Phys Rev Lett* 118.

Lim, T.C., Farnell, G.W., 1969. Character of Pseudo Surface Waves on Anisotropic Crystals. *The Journal of the Acoustical Society of America* 45, 845-851.

Lin, F., Ullah, S., Yang, Q., 2020. Ultrafast vortex microlasers based on bounded states in the continuum. *Sci Bull* 65, 1519-1520.

Lyapina, A.A., Pilipchuk, A.S., Sadreev, A.F., 2018. Trapped modes in a non-axisymmetric cylindrical waveguide. *J Sound Vib* 421, 48-60.

Marinica, D.C., Borisov, A.G., Shabanov, S.V., 2008. Bound States in the continuum in photonics. *Phys Rev Lett* 100, 183902.

Matsubara, H., Yoshimoto, S., Saito, H., Jianglin, Y., Tanaka, Y., Noda, S., 2008. GaN Photonic-Crystal Surface-Emitting Laser at Blue-Violet Wavelengths. *Science* 319, 445-447.

Maznev, A.A., Every, A.G., 2018. Bound acoustic modes in the radiation continuum in isotropic layered systems without periodic structures. *Phys Rev B* 97.

Minkov, M., Williamson, I.A.D., Xiao, M., Fan, S., 2018. Zero-Index Bound States in the Continuum. *Phys Rev Lett* 121, 263901.

Noda, S., Yokoyama, M., Imada, M., Chutinan, A., Mochizuki, M., 2001. Polarization Mode Control of Two-Dimensional Photonic Crystal Laser by Unit Cell Structure Design. *Science* 293, 1123-1125.

Parker, R., Griffiths, W.M., 1968. Low frequency resonance effects in wake shedding from parallel plates. *J Sound Vib* 7, 371-379.

Plotnik, Y., Peleg, O., Dreisow, F., Heinrich, M., Nolte, S., Szameit, A., Segev, M., 2011. Experimental Observation of Optical Bound States in the Continuum. *Phys Rev Lett* 107, 183901.

Romano, S., Zito, G., Lara Yépez, S.N., Cabrini, S., Penzo, E., Coppola, G., Rendina, I., Mocellaark, V., 2019. Tuning the exponential sensitivity of a bound-state-in-continuum optical sensor. *Opt Express* 27, 18776-18786.

Rose, J.L., 1999. *Ultrasonic waves in solid media*. Cambridge University Press 10.

Rupin, M., Lemoult, F., Lerosey, G., Roux, P., 2014. Experimental demonstration of ordered and

- disordered multiresonant metamaterials for lamb waves. *Phys Rev Lett* 112.
- Rupin, M., Roux, P., 2017. A multi-wave elastic metamaterial based on degenerate local resonances. *J Acoust Soc Am* 142, EL75.
- Trzupek, D., Zieliński, P., 2009. Isolated True Surface Wave in a Radiative Band on a Surface of a Stressed Auxetic. *Phys Rev Lett* 103, 075504.
- von Neumann, J., Wigner, E.P., 1993. Über merkwürdige diskrete Eigenwerte, in: Wightman, A.S. (Ed.), *The Collected Works of Eugene Paul Wigner: Part A: The Scientific Papers*. Springer Berlin Heidelberg, Berlin, Heidelberg, pp. 291-293.
- Yang, X., Kim, Y.Y., 2018. Asymptotic theory of bimodal quarter-wave impedance matching for full mode-converting transmission. *Phys Rev B* 98, 144110.
- Yang, X., Kweun, M., Kim, Y.Y., 2019. Monolayer metamaterial for full mode-converting transmission of elastic waves. *Appl Phys Lett* 115, 071901.
- Yanik, A.A., Cetin, A.E., Huang, M., Artar, A., Mousavi, S.H., Khanikaev, A., Connor, J.H., Shvets, G., Altug, H., 2011. Seeing protein monolayers with naked eye through plasmonic Fano resonances. *Proceedings of the National Academy of Sciences* 108, 11784-11789.
- Zhen, B., Chua, S.-L., Lee, J., Rodriguez, A.W., Liang, X., Johnson, S.G., Joannopoulos, J.D., Soljačić, M., Shapira, O., 2013. Enabling enhanced emission and low-threshold lasing of organic molecules using special Fano resonances of macroscopic photonic crystals. *Proceedings of the National Academy of Sciences* 110, 13711-13716.
- Zhen, B., Hsu, C.W., Lu, L., Stone, A.D., Soljačić, M., 2014. Topological Nature of Optical Bound States in the Continuum. *Phys Rev Lett* 113, 257401.
- Zheng, M., Park, C.I., Liu, X., Zhu, R., Hu, G., Kim, Y.Y., 2020. Non-resonant metasurface for broadband elastic wave mode splitting. *Appl Phys Lett* 116, 171903.